

Snow Water Equivalent (SWE) is a key parameter in hydrological, climatological and meteorological applications. New efforts for spaceborne radar-based SWE retrieval algorithms are under development and this paper shows the capability of such retrievals using snow-physical model driven by meteo data, radiative transfer and Bayesian inference. This paper focuses on the SWE retrieval framework leveraging previous work. The paper shows the readiness and capabilities of combining existing models and products to produce a SWE retrieval for RADAR data. The paper is well constructed and provides great results for SWE retrievals using Ku band radar. The method is repeatable elsewhere and estimating the background with X-band is clever.

Refining and thinning the results section would help clarify the take home message. Most of the figures are almost duplicates and I'm not sure I see the benefit in most cases. Or it is not well explained in the text. I have specific comments throughout the paper.

Specific comments:

Line 73-75 : This is a key sentence in setting the objective but it's complicated to understand. I suggest reformulating.

Line 76: Do you need all the verb? I feel like *propose* and *evaluate* were enough. Previous studies already implemented and demonstrated.

Line 83: temporal variability relates to temporal resolution of the orbit or revisit time of the satellite. I suggest removing or adding high temporal resolution higher.

Line 86 : "a coupled multi-layer snow hydrology model"? add model

Line 127 and line 130: Should it be y not x for the retrieved variable?

Line 148 and Line 150: do we maximize $P(n|y)$ or $P(y|n)$?

Line 164 : I suggest a bit more detail in the paragraph. Is y the snow depth, SWE or backscatter? Did you use the likelihood ratio to iterate in the MCMC like Pan et al?

Line 246. Wrong figure number. Should be 6.

Figure 5 : Is this the layer index? What does 15 layers mean? Top or bottom? Height or normalized height would be better. Put density on the x-axis.

Line 267: Why this value? Can you explain more this parameter. "This is an empirical factor that ..."

Line 271: replace microphysics for microstructure.

Line 272: add the symbol (l_{ex}) that represent the correlation length in MEMLS.

Table 2: Relates to the previous comment. Why use D?. D is the equivalent grain size used in DMRT. Replace D for l_{ex} .

Line 298: "for each layers"

Figure 6: The figure could be clearer. Later you refer to steps, but no steps are indicated in the figure. Pretty hard to understand even if you know Bayesian SWE retrieval. This could improve the understanding of the reader.

Line 317: It is not clear how the background is estimated. Maybe Specified that the volume is modelled from MSHM in the text not just in figure 6. Then explain why only using X band. It might not be obvious to someone not familiar with the fact that X band is more sensitive to the background than Ku.

Line 358 : "toweak" change "to a weak"

Figure 8 : I don't see the point of having 4 columns in the figure and then another figure for Ku. Can your aggregate heatmap for all dates and have x and ku in the same figure? They all look the same. I think we get the idea that the backscatter converges to the observed.

Line 471: remove in after between.

Line 475: add a coma after "In all cases".

Table 6: change title to " Same as Table 5 but for resolution = 90 m".

Line 529 – 530: Can you add the mean values stated here in the table as the last row?

Table 5, 6, 7 and 9: Any benefit in having the same table but with different resolutions? We get the idea in Table 4 regarding the resolution. Just make the point you want and move on. There is no point in having both figure 12 and 13. Just show one. I don't see any big conclusion regarding the resolution so there is no point in adding extra figures and tables.

Reply To Reviewer 1

We thank the Reviewer for the helpful comments and suggestions. The Reviewer's comments are in black. Our replies are in blue.

Snow Water Equivalent (SWE) is a key parameter in hydrological, climatological and meteorological applications. New efforts for spaceborne radar-based SWE retrieval algorithms are under development and this paper shows the capability of such retrievals using snow-physical model driven by meteo data, radiative transfer and Bayesian inference. This paper focuses on the SWE retrieval framework leveraging previous work. The paper shows the readiness and capabilities of combining existing models and products to produce a SWE retrieval for RADAR data. The paper is well constructed and provides great results for SWE retrievals using Ku band radar. The method is repeatable elsewhere and estimating the background with X-band is clever.

Thank you.

Refining and thinning the results section would help clarify the take home message. Most of the figures are almost duplicates and I'm not sure I see the benefit in most cases. Or it is not well explained in the text. I have specific comments throughout the paper.

We made a conscientious effort to eliminate duplicates in the main paper and revised the manuscript for clarity.

Specific comments:

Line 73-75 : This is a key sentence in setting the objective but it's complicated to understand. I suggest reformulating.

Line 73 is Line 80 in the revised manuscript: Sentence was revised and references were added.

Line 76: Do you need all the verb? I feel like *propose* and *evaluate* were enough. Previous studies already implemented and demonstrated.

Line 76 is Line 83 in the revised manuscript: Revised.

Line 83: temporal variability relates to temporal resolution of the orbit or revisit time of the satellite. I suggest removing or adding high temporal resolution higher.

Line 83 is Line 89 in the revised manuscript: Removed the temporal reference as suggested.

Line 86 : "a coupled multi-layer snow hydrology model"? add model

Line 86 is Line 92 in the revised manuscript: Revised.

Line 127 and line 130: Should it be y not x for the retrieved variable?

Line 127 is Line 133 in the revised manuscript: Point well taken. Section 2.2 was carefully edited for clarity. We start with general indirect measurements D to pose the general problem, and then for a specific instrument we replace D by y . η includes the geophysical variables x as well as the model parameters.

Line 148 and Line 150: do we maximize $P(\eta|y)$ or $P(y|\eta)$?

Line 148 is Line 154 in the revised manuscript: To maximize $P(\eta|y)$ we need to maximize $P(y|\eta)$ since $P(\eta)$ is a prior probability. This should be clearer after the editing.

Line 164 : I suggest a bit more detail in the paragraph. Is y the snow depth, SWE or backscatter? Did you use the likelihood ratio to iterate in the MCMC like Pan et al?

Line 164 is Line 167 in the revised manuscript: Yes. This was added to the text.

Line 246. Wrong figure number. Should be 6.

Line 246 is Line 272 in the revised manuscript: Yes. Thank you. This was corrected.

Figure 5 : Is this the layer index? What does 15 layers mean? Top or bottom? Height or normalized height would be better. Put density on the x-axis.

Figure 5 is Figure 6 in the revised manuscript: The layering scheme in MSHM is from bottom to top following the evolution of the snowpack during the accumulation. The higher index layer is the top layer; the bottom layer is always the first layer.

We switched the axis in Figure 5 to have density in the x-axis which is a more intuitive way to visualize the density profile of the snowpack as suggested by the Reviewer. The figure caption was also improved for clarity and detail.

Line 267: Why this value? Can you explain more this parameter. "This is an empirical factor that ..."

Line 267 is Line 292 in the revised manuscript: Revised as suggested.

Line 271: replace microphysics for microstructure.

Line 271 is Line 297 in the revised manuscript: Revised as suggested.

Line 272: add the symbol (l_{ex}) that represent the correlation length in MEMLS.

Line 272 is Line 299 in the revised manuscript: Revised as suggested.

Table 2: Relates to the previous comment. Why use D?. D is the equivalent grain size used in DMRT. Replace D for l_{ex} .

There was a notation confusion between the snow grainsize and correlation length. This is fixed now.

Line 298: “for each layers”

Line 298 is Line 335 in the revised manuscript: Revised as suggested.

Figure 6: The figure could be clearer. Later you refer to steps, but no steps are indicated in the figure. Pretty hard to understand even if you know Bayesian SWE retrieval. This could improve the understanding of the reader.

Figure 6, now Figure 5, was completely revised with each step identified. We hope the workflow is clearer now.

Line 317: It is not clear how the background is estimated. Maybe Specified that the volume is modelled from MSHM in the text not just in figure 6. Then explain why only using X band. It might not be obvious to someone not familiar with the fact that X band is more sensitive to the background than Ku.

Done. This is now in Line 316. We added a reference to justify the choice of HH-pol and revised the sentence. As pointed out in Section 3, SnowSAR Ku HH-pol measurements are not reliable.

Line 358 : “toweak” change “to a weak”

Line 358 is Line 387 in the revised manuscript: Revised as suggested.

Figure 8 : I don't see the point of having 4 columns in the figure and then another figure for Ku. Can you aggregate heatmap for all dates and have x and ku in the same figure? They all look the same. I think we get the idea that the backscatter converges to the observed.

We understand the Reviewer's point. Each heatmap synthesizes independent retrievals over different flight paths and thus for different viewing geometries. Because of the importance of showing the robustness of the algorithm, we prefer to keep the results. We did revise the figure to make it easier to read and less crowded. We hope this is acceptable.

Line 471: remove in after between.

Line 471 is Line 493 in the revised manuscript: Revised as suggested.

Line 475: add a coma after “In all cases”.

Line 475 is Line 498 in the revised manuscript: Revised as suggested.

Table 6: change title to “ Same as Table 5 but for resolution = 90 m”.

Done. Tabel was moved to Appendix as Table A1.

Line 529 – 530: Can you add the mean values stated here in the table as the last row?

Line 529 is Line 521 in the revised manuscript: Revised as suggested.

Table 5, 6, 7 and 9: Any benefit in having the same table but with different resolutions? We get the idea in Table 4 regarding the resolution. Just make the point you want and move on. There is no point in having both figure 12 and 13. Just show one. I don't see any big conclusion regarding the resolution so there is no point in adding extra figures and tables.

The Reviewer's point is well taken. Figures and Tables for 90 m resolution were moved to Appendix.

Thank you.

1 **BAYESIAN PHYSICAL-STATISTICAL RETRIEVAL OF SWE AND SNOW DEPTH FROM X**
2 **AND KU-BAND SAR - DEMONSTRATION USING AIRBORNE SNOWSAR IN SNOWEX'17**

3 Siddharth Singh¹, Michael Durand,² Edward Kim³, Ana P. Barros¹

4
5 ¹Department of Civil and Environmental Engineering, University of Illinois at Urbana-
6 Champaign, Urbana, Illinois, USA

7 ²School of Earth Sciences, Ohio State University, Columbus, Ohio, USA

8 ³NASA Goddard Space Flight Center, Greenbelt, Maryland, USA

9 *Correspondence to:* Ana P. Barros (barros@illinois.edu)

10 **Abstract**

11 A physical-statistical framework to estimate Snow Water Equivalent (SWE) and snow depth from
12 SAR measurements is presented and applied to four SnowSAR flight-line data sets collected
13 during the SnowEx'2017 field campaign in Grand Mesa, Colorado, USA. The physical (radar)
14 model is used to describe the relationship between snowpack conditions and volume backscatter.
15 The statistical model is a Bayesian inference model that seeks to estimate the joint probability
16 distribution of volume backscatter measurements, snow density and snow depth, and physical
17 model parameters. Prior distributions are derived from multilayer snow hydrology predictions
18 driven by downscaled numerical weather prediction (NWP) forecasts. To reduce noise to signal
19 ratio, SnowSAR measurements at 1 m resolution were upscled by simple averaging to 30 and 90
20 m resolution. To reduce the number of physical parameters, the multilayer snowpack is
21 transformed for Bayesian inference into an equivalent single- or two-layer snowpack with the same
22 snow mass and volume backscatter. Successful retrievals meeting NASEM (2018) science
23 requirements are defined by absolute convergence backscatter errors ≤ 1.2 dB and local SnowSAR
24 incidence angles between 30° and 45° for X- and Ku-band VV-pol backscatter measurements and
25 were achieved for 75% to 87% for all grassland pixels with SWE up to 0.7m and snow depth up
26 to 2 m.. SWE retrievals compare well with snow pit observations showing strong skill in deep
27 snow with average absolute SWE residuals of 5-7% (15-18%) for the two-layer (single-layer)
28 retrieval algorithm. Furthermore, the spatial distributions of snow depth retrievals vis-à-vis LIDAR
29 estimates have Bhattacharya Coefficients above 94% (90%) for homogeneous grassland pixels at
30 30 m (90 m resolution), and values up to 76% in mixed forest and grassland areas indicating that
31 the retrievals closely capture snowpack spatial variability. Because NWP forecasts are available
32 everywhere, the proposed approach could be applied to SWE and snow depth retrievals from a
33 dedicated global snow mission.

34

35 1. Introduction

36 The seasonal snowpack plays a critical role in climate and weather variability due to its role in the
37 surface energy budget on account of its high albedo, and in the surface water budget as temporary
38 storage of frozen precipitation in the cold season until it melts in the warm season and becomes
39 available as runoff. The water stored in the snowpack is measured by the Snow Water Equivalent
40 (SWE), the depth of liquid water per unit area that would be released if the snowpack were to melt
41 completely. It is the product of the specific gravity of snow with respect to water ($\rho_{\text{snow}}/\rho_{\text{w}}$) and
42 the depth of the snowpack (SD). To map SWE in the cold season is to map snow water resources.
43 To map onset of melt and snow wetness is to map the timing and geography of snow water
44 resources availability. Climate variability and change with increasing air temperature, shifts in
45 atmospheric moisture convergence patterns, and increases in the frequency of extreme events is
46 already causing significant changes in frequency and patterns and timing of seasonal snow
47 accumulation and melt with severe implications for water and food security in addition to
48 cascading economic and ecosystem impacts (Huang and Swain, 2022; Musselman et al., 2021;
49 Sturm et al., 2010).

50 The need to capture snowpack heterogeneity and dynamics tied to weather, climate, landcover and
51 landform variability remains a chief challenge to developing a snow observing system at the spatial
52 and temporal scales required to answer water cycle science questions and for societal decision-
53 making. The potential for systematic snowpack monitoring in remote regions has long been
54 investigated, including the integration of remote sensing measurements and physical models (e.g.
55 (Martinec et al. 1991; Mote et al. 2003; Bateni et al. 2015; Li et al. 2017; Kim et al. 2019; Cao and
56 Barros, 2023a). Assimilation of radiance or backscatter is most powerful with a time series of
57 observations. Time-series observations are available presently from tower measurements, albeit
58 at the point scale of the tower footprint (see summary by Tsang et al. 2022), and do not capture
59 the large joint spatial and temporal variability of snowpacks from local to regional scales
60 depending on weather and climate, landform, land use and landcover. Frequent spatial
61 observations are required for this purpose. Airborne observations can be used for mapping but
62 typically occur once or twice during a winter season and over limited areas. A dedicated satellite
63 mission is necessary to acquire time-series of measurements globally.

64 Presently, advances in radar technology and retrieval algorithms (Tsang et al., 2022), and
65 especially the demonstrated capabilities of NewSpace satellite missions (Villano et al. 2020) make
66 high spatial resolution of Synthetic Aperture Radar (SAR; 10's m) Earth observations from space
67 feasible in contrast to the challenges faced in the past (Rott et al. 2012). During the SnowEx'17
68 field campaign (Kim et al., 2017), a comprehensive data set consisting of airborne dual-frequency
69 SAR (X- and Ku-band Synthetic Aperture Radar) backscatter measurements using the SnowSAR
70 instrument (Macedo et al. 2020), the Airborne Snow Observatory (ASO, Painter et al. 2018) and a
71 plethora of high-quality ground-validation measurements of snowpack properties and ancillary
72 data (Table 1) offer an unprecedented opportunity to investigate the full potential of SAR toward
73 developing the next generation of retrieval algorithms.

74 Due to the highly nonlinear snow physics and the time-varying stratigraphy of snowpacks,
75 radiance or backscatter measurements depend on the vertical structure of snowpack physical
76 properties such as snow density, snow temperature, and snow grain size in addition to SWE and

77 snow depth. Because the number of observations is smaller than the number of parameters required
78 to solve the inverse-problem, retrieval of SWE and snow depth is an underdetermined estimation
79 problem. This challenge can be addressed using a physical-statistical approach for retrieval.
80 Physical-statistical approaches combine physical process models with a Bayesian statistical
81 framework to inform how geophysical states and parameters relate to measurements by obeying
82 fundamental physical constraints (Berliner, 2003; Lowman and Barros, 2014). In this manuscript,
83 we propose, and evaluate a general physical-statistical framework to retrieve SWE from SnowSAR
84 measurements across a heterogeneous landscape during SnowEx'17.

85

86 **2. Previous Work**

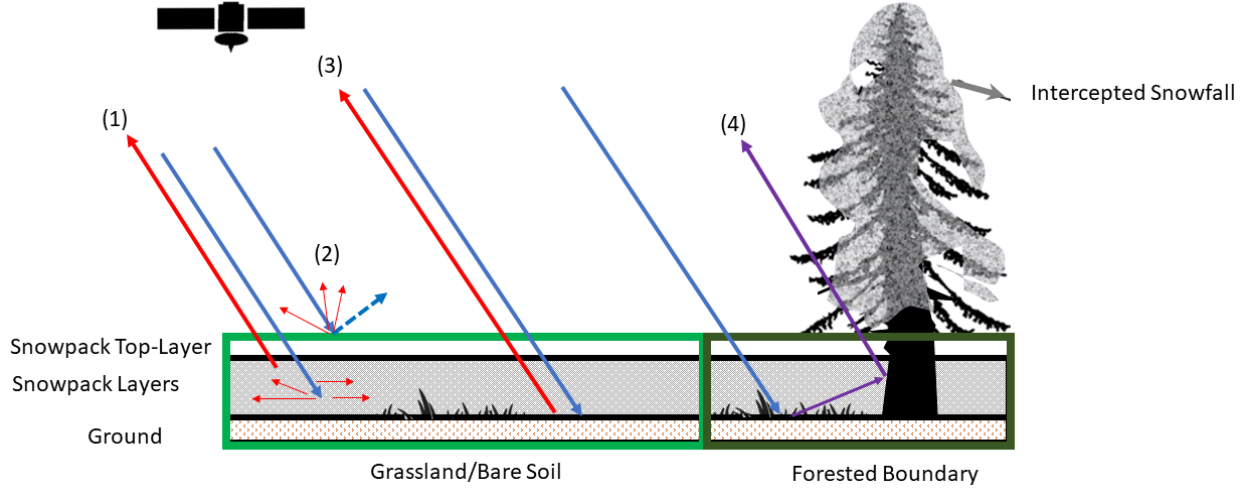
87 **2.1 Forward Simulation - From SWE to Backscatter**

88 The advantage of SAR technology is the high-spatial resolution of its measurements, which is
89 necessary to capture the spatial heterogeneity of snowpack physical processes (e.g. Deems et al.
90 2016; Mendoza et al., 2020; Manickam and Barros, 2020) as demonstrated in forward simulations.
91 Cao and Barros (2020, 2023a; hereafter CB20 and CB23) demonstrated the utility of a multi-layer
92 snow hydrology (MSHM) coupled with a radiative transfer model (RTM) forced by high-
93 resolution operational numerical weather prediction (NWP) model forecasts to capture the
94 seasonal hysteresis behavior of the seasonal snowpack at Grand Mesa and Senator Beck in
95 Colorado against Sentinel-1 C-band measurements.

96 The MSHM is a physically driven snow hydrology model that simulates the evolution of snowpack
97 physical properties including detailed stratigraphy (Kang and Barros, 2012a-b; CB20). During
98 snowfall events, fresh snow is added to the top layer of the snowpack until a threshold
99 accumulation is met, and a new layer forms. The RTM used here is MEMLS3a (Microwave
100 Emission Model of Layered Snowpacks adapted to include backscattering by Proksch et al., 2015).
101 MEMLS is a physically driven radiative transfer model which takes snowpack characteristics as
102 inputs and simulates its microwave emission for a frequency band with four polarizations – HH,
103 VV, HV and VH (originally proposed by Wiesmann and Mätzler, 1999). To estimate total
104 scattering, ground backscatter σ_{bkg} must be modeled as well, as described below. .

105 Figure 1 illustrates the various backscatter mechanisms contributing to total backscatter (σ_{total}) in
106 active microwave measurements represented in MEMLS3&a, the RTM: volume backscatter (σ_{vol})
107 from the multiple interactions of the incoming radar signal within the snowpack, the backscatter
108 at the snowpack-air interface (σ_{surf}) and at the snowpack-ground interface including interactions
109 with submerged vegetation and litter (σ_{bkg}). In forested areas, additional backscatter mechanisms
110 are associated with the multiple bounce pathways among tree canopy, intercepted snow, tree
111 trunks, and snowpack. Depending on viewing geometry (flight path and incidence angle), σ_{total}
112 measurements from areas without trees in regions of mixed landcover can include significant
113 contribution from trees along the grassland-forest transitions.

114



115

116 **Figure 1:** Scattering mechanisms for grassland submerged by snow and snowpack over bare soil or rock: (1) Volume Backscatter
 117 σ_{vol} ; (2) surface backscatter σ_{surf} ; (3) background backscatter at the snow-ground interface σ_{bkg} ; (4) snowpack-ground-canopy-tree
 118 trunk interactions at forested boundaries. Red arrows (1), (2) and (3) are resolved in the retrieval applications demonstrated here.

119

120 CB23 used the coupled MSHM-MEMLS in forward mode to predict Sentinel-1 C-band volume
 121 backscatter σ_{vol} without calibration or nudging of ground observations without bias and within \pm
 122 2.5 dB at 90 m resolution across terrain slopes in the $[10^\circ-52^\circ]$ range for barren land, alpine grass
 123 and shrubs and in forested areas with snow-free canopy at the beginning of spring in the Senator
 124 Beck Basin in Colorado. They estimated σ_{bkg} as the average of Sentinel-1 measurements for
 125 snow-free conditions. Cao and Barros (2023b) modified MEMLS3&a to include double-bounce
 126 effects among snowpack and vegetation (MEMLS-V) and retrieved σ_{bkg} from total backscatter
 127 σ_{total} measurements in mixed landcover using simulated annealing. Their estimates are consistent
 128 with CB23, suggesting potential to simplify the inverse-problem of estimating snowpack physical
 129 properties from total backscatter measurements in mixed landcover and further simplify the
 130 physical-statistical retrieval framework proposed here, although further evaluation is necessary.

131

132 2.2 Physical-Statistical Retrieval

133 For retrieval in a Bayesian framework, the probability of the retrieved geophysical variable x (the
 134 inferred posterior distribution) is conditional on the *a priori* knowledge of the variable x (the prior
 135 distribution), indirect measurements D , and a physical model $M(\eta)$ (e.g., the snow radiative
 136 transfer algorithm in this case) with physical parameters η (including x) and statistical error
 137 parameters ζ . The joint probability distribution of M, D, η , and ζ can be written as:

$$138 \quad P(M, D, \eta, \zeta) = P(D|M, \eta, \zeta) \times P(M|\eta, \zeta) \times P(\eta, \zeta) \quad (1)$$

139 The first term to the right-hand side of Eq. (1) is the backscatter data model, the second term is the
 140 prior of the backscatter, and the third term is the prior of the snowpack physical parameters
 141 (including snow depth and snow density, etc) with statistical error parameters. Assuming the

142 measurements do not depend on the physical parameters, the model does not depend on the
 143 statistical error parameters, and that the physical parameters and the statistical parameters are
 144 independent, Eq. (1) can be revised to read

$$145 \quad P(M, D, \eta, \zeta) = P(D|M, \eta) \times P(M|\eta) \times P(\eta) \times P(\zeta) \quad (2)$$

146 And finally in the context of specific measurements y with known uncertainty described by $P(y)$

$$147 \quad P(M, \eta, \zeta | y) = P(y|M, \eta) \times P(M|\eta) \times \frac{P(\eta) \times P(\zeta)}{P(y)} \quad (3)$$

150 The physical model M and $P(y)$ are invariant and assuming that we have a good understanding of
 151 the statistical errors, then Eq. (3) can be further simplified as follows

$$152 \quad P(\eta|y) \propto P(y|\eta) \times P(\eta) \quad (4)$$

153
 154 In the context of Bayesian inference the goal is to maximize $P(\eta|y)$, the posterior probability of
 155 physical parameters conditional on measurements informed by the a priori parameter probabilities
 156 $P(\eta)$. This implies maximizing the second term in Eq.(4), the posterior of the backscatter
 157 conditional on physical parameters η , implies minimizing the difference between measurements y
 158 with known error covariance matrix Σ_y and model predictions $M(\eta)$. For multiple concurrent
 159 measurements, $P(y|\eta)$ can be described by a multivariate normal distribution,

$$160 \quad P(y|\eta) = (2\pi)^{\left(-\frac{N}{2}\right)} |\Sigma_y|^{-\frac{1}{2}} \exp\left[-\frac{1}{2}(y - M(\eta))^T \Sigma_y^{-1}(y - M(\eta))\right] \quad (5)$$

161 where N is the number of measurements at a given location and time (e.g. backscatter at different
 162 frequencies as in Durand and Liu, (2012).

163 Pan et al. (2023, hereafter P23) adapted a Bayesian retrieval algorithm previously developed to
 164 estimate SWE from passive microwave measurements (Pan et al. 2017, hereafter P17) to active
 165 microwave, hereafter referred to as Base-AM. The snow radiative transfer algorithm in Base-AM
 166 is MEMLS, and the semi-empirical Dobson model is used to estimate the soil dielectric constant
 167 as a function of soil moisture and soil texture (Dobson et al. 1985; Hallikainen et al. 1985). A
 168 Monte Carlo Markov Chain (MCMC) iterative algorithm (Metropolis et al. 1953) is used to sample
 169 from $P(\eta|y)$ starting from initial values and using the likelihood ratio criteria to achieve
 170 convergence. In this work, realistic snowpack predictions from MSHM-MEMLS are used to
 171 define the prior distributions of parameters and constrain the Bayesian retrievals: y represents the
 172 SnowSAR backscatter measurements and η represents to all model parameters and geophysical
 173 variables including SWE, SD, snow density.

174

175 **3. Study Area and Data**

176 **3.1 Study Area and Ancillary Data**

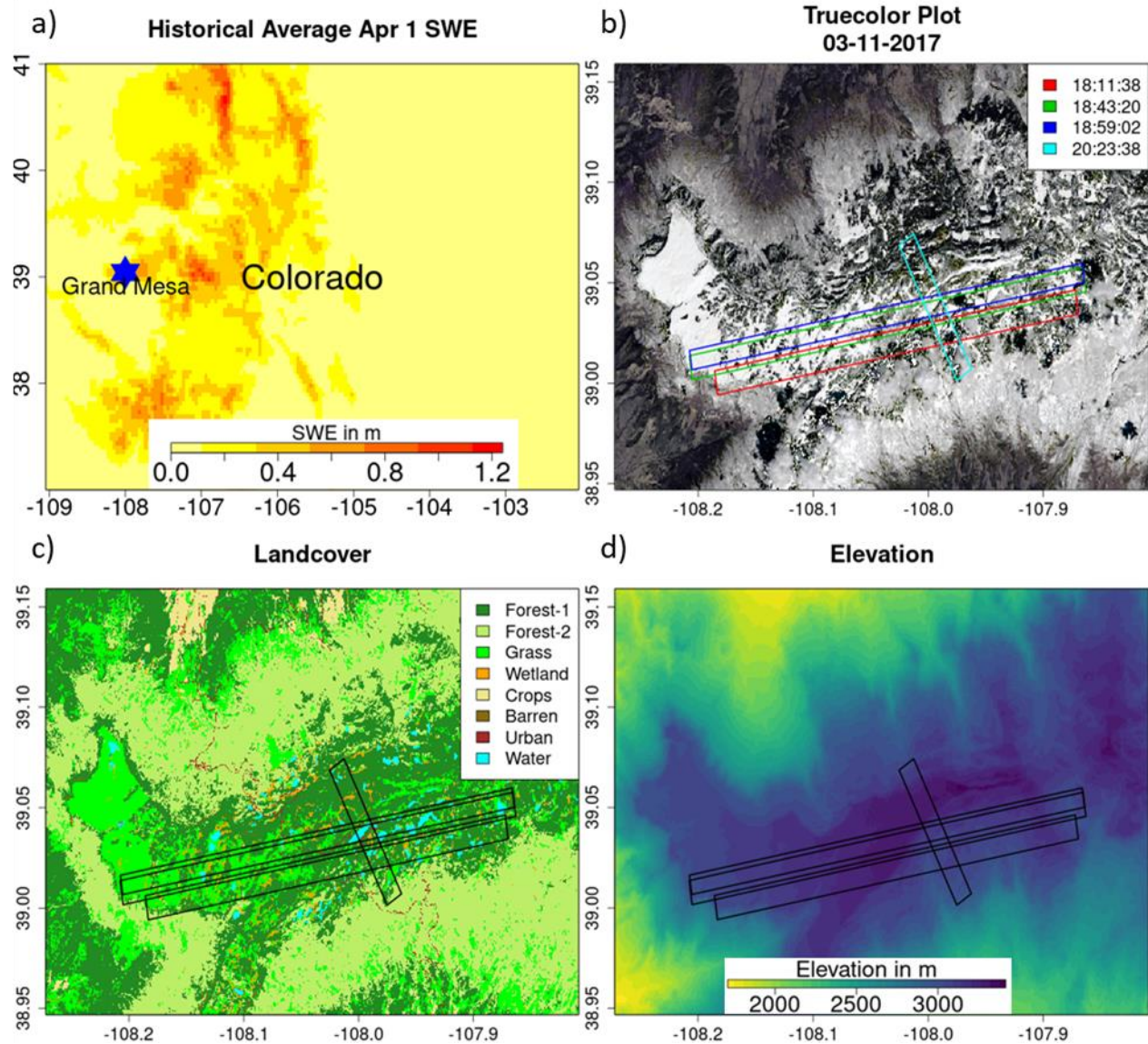
177 The study region is Grand Mesa, Colorado, a plateau that is 2,000 m above adjacent low-lying
 178 areas and is surrounded by ridges up to 500m in elevation (as depicted in Fig. 2). Grand Mesa
 179 has an alpine climate, experiencing snowfall throughout the year except during the months of July
 180 and August. Landcover is heterogeneous with grasslands in the west and a mix of evergreen and
 181 deciduous forest to the east. Numerous wetlands are widespread across the Mesa, especially in the
 182 transition from grassland to forest. The land cover data were obtained from the National Land Data
 183 Assimilation System (NLDAS). The datasets were upscaled to 90 m using nearest neighbor
 184 interpolation to support retrievals at 90 m resolution (see Section 4). NLDAS is used to determine
 185 landcover type in the snow hydrology model. NALCMS is used to upscale the evaluation data.
 186 Hourly albedo is derived from NLDAS at 12.5 km resolution. A summary of all the datasets used
 187 in this study is available in Table 1.

188

189 **Table 1:** Summary list of datasets used in the study.

Data	Source	Spatial Resolution		Temporal Resolution		Date Range	Relevant Link
		Initial	Final	Initial	Final		
Rainfall Temperature Air Pressure Incoming SW radiation Incoming Longwave radiation Wind speed Humidity	HRRR	3 km	30 m, 90 m	1 hr	30 min	9/1/2016 - 2/25/2017	https://rapidrefresh.noaa.gov/hrrr/
Albedo	NLDAS	12.5 km	30 m	1 hr	30 min	9/1/2016-2/25/2017	https://ldas.gsfc.nasa.gov/
Backscatter	SnowSAR – SnowEx’17	1 m	30 m, 90 m	-	-	2/21/2017	https://nsidc.org/data/snex17_snowsar/versions/1
Landcover	NLCD, NALCMS	30 m	30 m, 90 m	-	-	-	https://www.usgs.gov/centers/eros/science/national-land-cover-database http://www.cec.org/north-american-land-change-monitoring-system/
Snow Depth	LIDAR – SnowEx’17	3 m	30 m, 90 m	-	-	2/25/2017	https://nsidc.org/data/aso_3m_sd/versions/1
SWE	Snowpit – SnowEx’17	-	-	-	-	2/20/2017-2/24/2017	https://nsidc.org/data/snex17_snowpits/versions/1

190



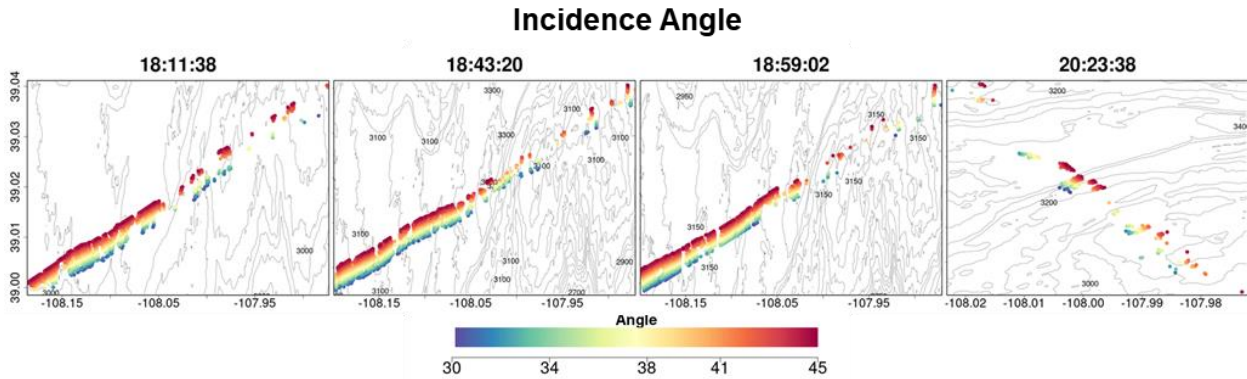
191
 192 **Figure 2:** Study area in Grand Mesa, Colorado. a) Location of Grand Mesa in Colorado, with historical Apr 1 SWE average as
 193 base map. b) Paths of 4 SnowSAR SnowEx'17 flights on 21 Feb 2017, with true color image obtained from Landsat on 03/11/2017
 194 as the base map. c) Land cover of the study region. Forest-1 are needle leaf forests; Forest-2 are broadleaf forests. d) Digital
 195 elevation map of the study region.

196

197 3.2 Atmospheric Forcing

198 Numerical Weather Prediction (NWP) outputs are used as the atmospheric forcing for the snow
 199 hydrology model and to set up boundary conditions. Previously, CB20 and CB23 relied on HRRR
 200 (High-Resolution Rapid Refresh) hourly forecasts at 3 km and downscaled it to 90 m in Grand
 201 Mesa. Here, the same data set was independently downscaled to 30 m as well. The HRRR dataset
 202 is produced by National Ocean and Atmospheric Agency (NOAA) by hourly assimilation of
 203 observations at 13 km resolution (Benjamin et al., 2016; Table 1). Hourly atmospheric forcing
 204 was linearly interpolated to 30 min temporal resolution used in the snow hydrology model.

205



206

207 **Figure 3:** Maps of incidence angles along SnowSAR flight paths on February 21, 2017 during SnowEx'17.

208

209 3.3 SnowSAR Backscatter

210 During SnowEx'17, airborne microwave backscatter measurements were made in Grand Mesa on
211 21 Feb 2017 at 1 m resolution (Table 1). The SnowSAR instrument is a dual frequency (X and Ku
212 Band) radar. A total of six flightlines were completed, two short ones on sloped densely forested
213 terrain and four long lines on the plateau. Here, only the four flightlines on the plateau are used for
214 analysis (Fig. 2 and Fig. 3). The flights are between 18:00 and 21:00 GMT (noon – 3PM MST).
215 SnowSAR data quality control measures included filtering based on aircraft attitude (there were
216 line segments with turbulence), beam incidence angle/antenna pattern, and signal-to-noise-ratio of
217 the backscatter coefficients. Processing of the original airborne SAR measurements and quality
218 control indicate that only the co-pol X-band HH- and VV-pol as well as Ku-band VV-pol
219 measurements are adequate for retrieval. Geolocation was verified against corner reflector targets
220 and geographic features and found to be very robust. The SnowSAR data were upscaled to 30 m
221 and 90 m resolution by simple averaging of all SnowSAR measurements within each pixel.

222

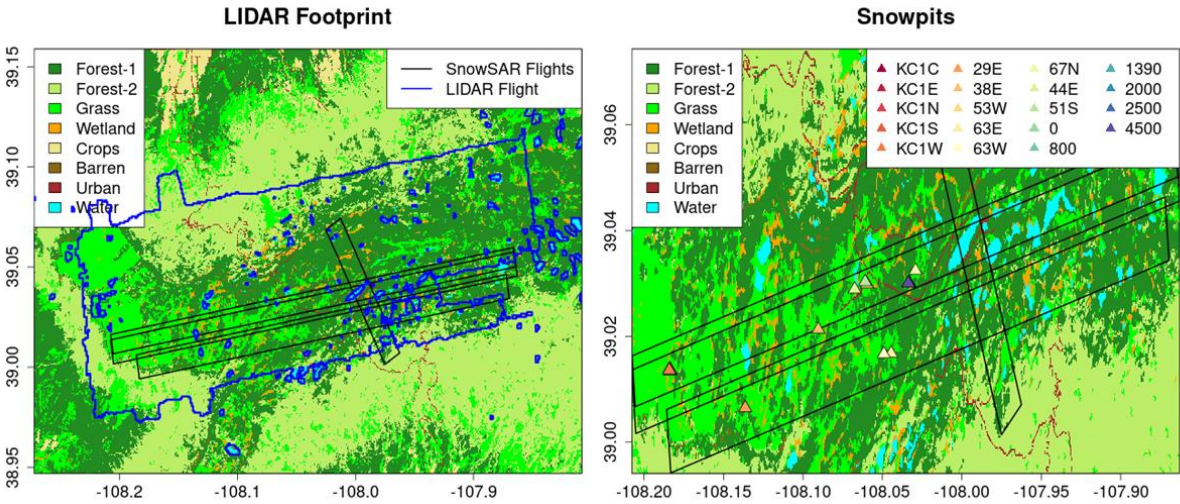
223 3.4 Validation Data

224 *LIDAR Snow Depth* – The Airborne Snow Observatory (ASO) LIDAR measurements of snow
225 depth at 3m resolution across Grand Mesa are available for SnowEx'17 on February 25, thus 4
226 days after the SnowSAR flights (Painter et al., 2018; Table 1). There were no significant snow
227 storms or strong winds in that period, except for about 3mm of rainfall for less than 1 hour on
228 February 24. These data are used to examine the distribution of retrieved snow depths, that is
229 indicative of the spatial heterogeneity of the snowpack, and the relative absolute differences
230 between LIDAR measurements and retrieval of snow depth, that are indicative of local retrieval
231 errors. The LIDAR data were upscaled to 30 m and 90 m using simple averaging (e.g., Fig.4a).
232 There can be large snow depth underestimation errors associated with upscaled LIDAR retrievals
233 along the edges of forests where the snow depth is underestimated consistent with previous work
234 (e.g. Deems et al. 2013; Jacobs et al. 2021). Given the expected measurement uncertainty on the

235 order of 10-20 cm in Grand Mesa, which is amplified by microtopography, LIDAR pixels with
236 snow depth shallower than 20 cm are not considered for evaluation.

237 *Snowpit SWE* - Multiple snowpits were excavated during the SnowEx'17 field campaign across
238 Grand Mesa (Table 1). Due to the small number of snow pit measurements along the SnowSAR
239 flightlines on 21 February, snowpit measurements on 20-24 of February were considered for
240 evaluation assuming that in the absence of snowstorms or other weather events the snow pack
241 does not change significantly during the 4-day period. Differences are expected at local places but
242 the overall spatial trends should be maintained such as the west-east gradient in snow depth. The
243 values of snowpit SWE are estimated using an average of the snow density measurements at
244 different depths applied to the entire snow depth. Only pits in the non-forested areas were selected
245 for evaluation (Fig. 4b).

246



247
248 **Figure 4:** a) Flight footprint of the LIDAR instrument used to measure the snow depth during SnowEx'17. b) Location of snow
249 pits used to measure SWE 20-24 Feb 2017. The legend identifies SnowEx'17 Pit IDs.

250

251 4. Retrieval Algorithm

252 Simplicity and computational efficiency are desirable attributes for an operational algorithm that
253 produces successful retrievals, here understood as meeting science uncertainty requirements and
254 latency adequate to meet applications needs defined by NASEM (2018). The retrieval
255 methodology builds on existing and well evaluated snow hydrology, radiative transfer, and
256 physical-statistical models (CB20,CB23, P17, P23) previously reviewed in Section 2. A list of
257 forcings and coupling variables and parameters among MSHM, MEMLS and Base-AM is
258 provided in Table 2.

259 Averaging is necessary to reduce the signal to noise ratio (SNR) in SnowSAR measurements at
260 their native resolution (Section 3.3). Because the highest spatial resolution of available ancillary
261 data sets is 30 m, the SnowSAR measurements were upscaled to 30 m to eliminate the need for

262 interpolation and, or downscaling that introduce further uncertainty. Following results by
 263 Manickam and Barros (2020), the algorithm was also applied at 90 m resolution consistent with
 264 the first scaling break identified in Sentinel-1 SAR backscatter. The implication of linear scaling
 265 behavior is that successful retrievals at 90 m resolution can subsequently be statistically downscaled
 266 with confidence, which has significant computational advantages. Further upscaling was not
 267 conducted because the number of pixels becomes very small given the available coverage of
 268 SnowSAR flights.

269

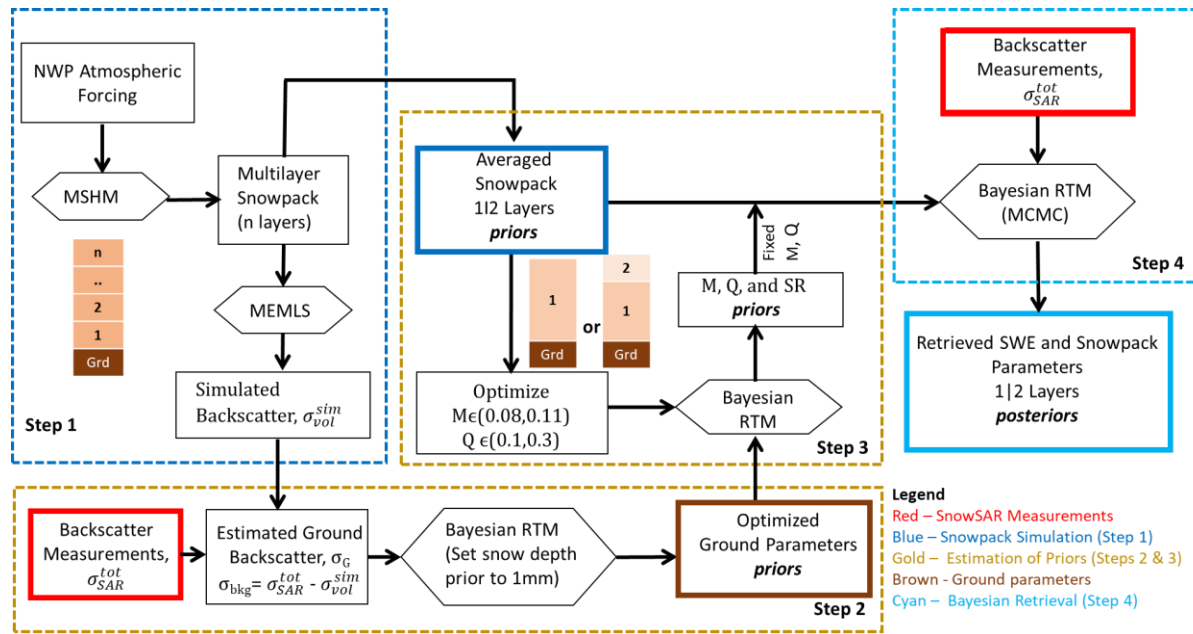
270 **Table 2:** Input and output parameters from the three models in the SWE physical-statistical retrieval framework.

Model	Input	Output	Reference
MSHM	Rainfall Temperature Air Pressure Incoming shortwave radiation Incoming longwave radiation Wind speed Humidity Albedo	Snow Temperature Profile Soil Temperature Profile Snow Density Profile Snow Depth Layering Profile Liquid Water Content Profile Snow Correlation Length Profile	Cao and Barros (2020)
MEMLS	Snow Temperature Profile Soil Temperature Profile Snow Density Profile Snow Depth Layering Profile Snow Correlation Length Profile Cross polarization fraction Ground rms height	Diffused Reflectivity Profile Specular Reflectivity Profile Total Backscatter Coefficient	Proksch et al. (2015)
Base-AM	Equivalent Snow Temperature Prior Equivalent Soil Temperature Prior Equivalent Snow Density Prior Equivalent Snow Depth Prior Correlation Length Cross polarization fraction Ground rms height Total Backscatter Coefficient Prior	Optimized – Snow Layer Depth Snow Density	Pan et al., (2023)

271

272 Figure 5 illustrates the retrieval workflow consisting of four main steps. **Step 1** - Snow hydrology
 273 simulation using MSHM to produce a layered snowpack and volume backscatter simulation using
 274 MEMLS (σ_{vol}^{sim}). **Step 2** - Bayesian estimation of ground parameter priors that govern background
 275 backscatter σ_{bkg} using MEMLS assuming a very thin film of snow on the ground (1 mm SD) at the
 276 beginning of the accumulation season and estimation of the σ_{bkg} by subtraction of σ_{vol}^{sim} from
 277 SnowSAR total backscatter measurements σ_{SAR}^{tot} . **Step 3** - Determination of snowpack priors for
 278 Bayesian SWE retrieval using results Step 1 and Step 2. **Step 4** - Bayesian optimization of
 279 simulated σ_{SAR}^{tot} to derive posterior distributions of SD and ρ_{snow} for the single- and two-layer (1|2)
 280 equivalent snowpack, and subsequent calculation of retrieved SWE posterior distributions

281



282

283 **Figure 5:** Workflow of the SWE Physical-Statistical retrieval framework. NWP atmospheric forcings drive MSHM to determine
 284 priors for the Bayesian radiative transfer model (Base-AM) and synthetic backscatter for ground parameters. SnowSAR backscatter
 285 measurements are assimilated to determine the posterior distribution of the snowpack parameters.

286

287 4.1 Layered Snowpack Simulations (Step 1)

288 Following the methodology presented in Section 2.1, MSHM was run for a full-year starting from
 289 snow free conditions on September 1st 2016 using downscaled HRRR data as atmospheric forcing
 290 (Section 3.2) and a timestep of 30 mins. On the day of the SnowSAR flights, the snowpack
 291 physical properties predicted at times corresponding to each of the four flights are used to derive
 292 the 1|2 Layer equivalent snowpack properties used in the retrieval. The simulated volume
 293 backscatter (σ_{vol}^{sim}) was estimated by specifying the cross polarization fraction parameter $Q=0.2$
 294 following CB20. This is an empirical coefficient that distributes the diffuse scattering into cross
 295 and like polarization components in MEMLS (Proksch et al. 2014).

296 In realistic layered snowpacks, stratigraphy (i.e., vertical heterogeneity) is a dominant feature of
 297 the density, temperature, microstructure, and dielectric properties (e.g., emissivity and
 298 reflectivity). The vertical structure of snow microstructure in MSHM is described using a
 299 parameterization of snow correlation length (l_{ex}) consistent with MEMLS formulation. Depending
 300 on the number of layers, this poses an undetermined problem as the number of measurements is
 301 equal to the number of frequencies and the number of polarizations available (typically two or
 302 three). For example, there are only four observations for a dual-frequency measurement with dual
 303 polarization. In contrast, the set of independent parameters per layer includes snow density, layer
 304 thickness, liquid water content, snow grain size or correlation length, temperature, reflectivity, and
 305 transmissivity.

306 While converting the multi-layer snowpack to a single-layer model is the simpler path to address
 307 the undetermined inverse-problem, fresh snowfall accumulation and snowpack crusting artifacts

308 due to melt-refreeze cycles, as well as hardening by wind action introduce strong density and grain
 309 size differences at the top of the snowpack. To capture this behavior, we implement and evaluate
 310 the retrieval algorithm for both single and two-layer equivalent snowpacks derived from the
 311 layered snowpack simulated by MSHM. The equivalent single- or two-layered snowpack
 312 parameters for each pixel are obtained by matching SWE, snow depth (SD) and volume backscatter
 313 (σ_{vol}^{sim}) of the simulated multilayer snowpack.

314

315 4.2 Ground and Snowpack Parameter Priors (Steps 2 and 3)

316 A first estimate of the σ_{bkg} is obtained by subtracting σ_{vol}^{sim} from SnowSAR X-band HH-pol
 317 σ_{SAR}^{tot} measurements following Baghdadi et al. (2011) who found better performance among
 318 backscattering models for HH-pol against TerraSAR-X measurements. In Base-AM, σ_{bkg} depends
 319 on the effective effective soil moisture and soil surface roughness. To optimize these parameters,
 320 σ_{bkg} is used as an “observed” value. To simulate snow-free conditions the snow depth is
 321 constrained to a maximum value of 1 mm in Step 2. The cross polarization fraction Q initially
 322 specified as Q=0.2 is optimized first and separately from other ground parameters in the third step
 323 of the retrieval algorithm (Fig. 5). The posterior distributions of the ground parameters in Step 2
 324 are used along with the 1|2 layer prior distributions and the SnowSAR measurements to estimate
 325 the posterior distributions of snow depth and snow density using the Base-AM framework (Fig. 5)
 326 and both X- and Ku-band VVpol. SWE is subsequently derived from snow depth and snow density.

327 *Single-layer Snowpack* - The total snow depth and the averages of multilayered snowpack
 328 parameters are specified as the mean of the prior distribution for retrieval. Table 3 shows the range
 329 and standard deviation of the parameters.

330

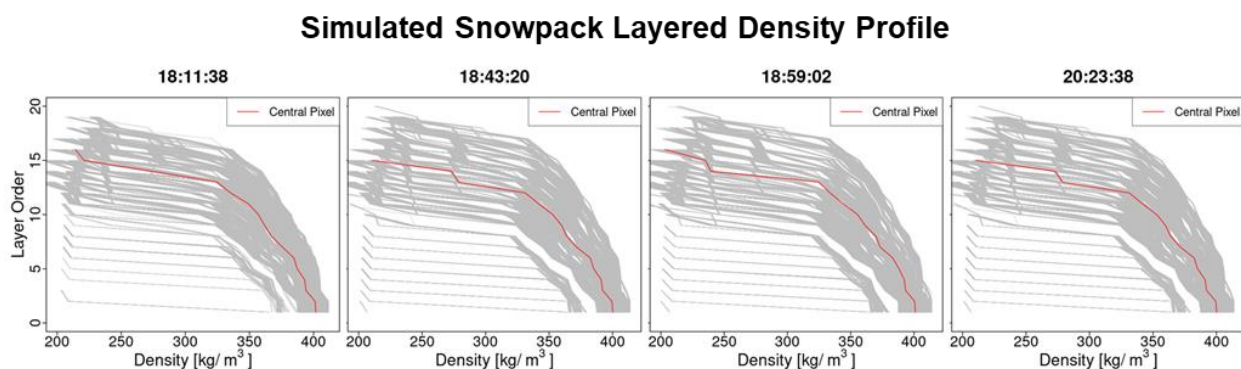
331 **Table 3:** Base-AM model input variance and range for the parameters prepared using MSHM multilayer snowpack parameters.
 332 Alphanumerical subscript in 2-layer snowpack retrievals denotes layer number: 1- bottom layer; 2- top layer; avg- the average of
 333 all MSHM multilayer parameter values in the corresponding single or 2-layer snowpack. DZ is the MSHM snow depth.

Snow Parameters	1 Layer Snowpack			2 Layer Snowpack			
	Variance, σ^2	Range		Variance, σ^2		Range for each layer	
		Min	Max	Bottom	Top	Min	Max
Snow Temp., Ts [$^{\circ}$ C]	$0.3 \times Ts_{avg}$	$1.3 \times Ts_{min}$	$0.7 \times Ts_{max}$	$0.3 \times Ts_{1,avg}$	$0.3 \times Ts_{2,avg}$	$1.3 \times Ts_{min}$	$0.7 \times Ts_{max}$
Snow Density, ρ [Kg/m ³]	$0.3 \times \rho_{avg}$	$0.8 \times \rho_{min}$	$1.2 \times \rho_{max}$	$0.3 \times \rho_{1,avg}$	$0.3 \times \rho_{2,avg}$	$0.8 \times \rho_{min}$	$1.2 \times \rho_{max}$
Snow Depth, DZ [m]	$0.3 \times DZ$	$0.5 \times DZ$	$1.5 \times DZ$	$0.1 \times DZ_1$	$0.2 \times DZ_2$	$0.2 \times DZ$	$0.9 \times DZ$
Correlation Length, l_{ex}	$0.3 \times l_{ex,avg}$	$l_{ex,min}$	$l_{ex,max}$	$0.2 \times l_{ex,1,avg}$	$0.2 \times l_{ex,2,avg}$	$l_{ex,min}$	$l_{ex,max}$
Soil Temp., Tsoil [$^{\circ}$ C]	0.3	1.3		0.3		1.3	

334

335 *Two-layer Snowpack* – The average values of the snowpack physical properties for each layer are
 336 derived from the multilayer snowpack simulated by MSHM. The key requirement is to determine
 337 the depth of each one of the layers that best captures the snowpack vertical structure. Figure 6
 338 shows MSHM simulated snowpack density profiles for each of the four SnowSAR flights. The
 339 shape of the profiles reflects the interplay between thermodynamic processes that change snow
 340 microstructure and dominate in the upper snowpack and mechanical consolidation processes that
 341 are dominant in the mid and lower layers. The snow depth point corresponding to the maximum
 342 change in snow density between adjacent layers in the multilayer snowpack is used here to divide
 343 the snowpack in two layers. Subsequently, the layer-depth weighted average density, snow
 344 temperature, and correlation length of the MSHM multilayer snowpack is calculated for the
 345 corresponding depths of the two-layer equivalent snowpack (Table 3).

346



347

348 **Figure 6** - Density profiles simulated by MSHM for all grassland pixels at 30 m resolution from the 4 SnowSAR flight paths. The
 349 density profile of the central pixel for each of the flights is marked in red. The snowpack layers are numbered from bottom to top
 350 tracking the evolution of simulated snowpack stratigraphy during the accumulation season. Note the significant difference between
 351 the top 2-3 layers and the deeper snowpack supporting the two-layer snowpack conceptual retrieval model.

352

353 **4.3 Bayesian Optimization (Step 4)**

354 Realistic snowpack predictions from MSHM driven by weather forecasts (Step 1) are used to
 355 define the prior distributions of snowpack parameters and constrain Base-AM (Steps 2 and 3) to
 356 infer the posterior distribution of snowpack parameters given the SnowSAR backscatter
 357 measurements (Step 4) as discussed in Section 2.2.

358 The local mean of the posterior distribution for each parameter is hereafter referred to as the
 359 retrieval result for each pixel. SD retrievals are evaluated against LIDAR snow depth including
 360 spatial patterns and gradients, and overall statistical structure using histograms. SWE retrievals
 361 derived from the posterior distributions of snow density and snow depth are evaluated against SWE
 362 measurements at snowpits (Section 3.4). Original LIDAR measurements were reprojected and
 363 coregistered with the SnowSAR retrievals. A comparative analysis was conducted to examine the
 364 dependence of retrievals on incidence angle and the subgrid scale variability was quantified in
 365 terms of the standard deviation of original LIDAR measurements within the upscaled pixel. The

366 amplitude error metrics are the mean, standard deviation, and mean absolute relative error
 367 (MARE):

$$368 \quad MARE = \frac{\sum_{i=1}^n |1 - R_i/O_i|}{N} \quad (6)$$

369 where O are observations and R are retrievals. The Bhattacharya coefficient (BC) is used to
 370 compare the spatial distributions of snow depth and backscatter. BC measures the similarity
 371 between two probability distributions p_1 and p_2 as follows (Bhattacharya, 1943)

$$372 \quad BC = \sum_{i=1}^N \sqrt{p_1(i)p_2(i)} \quad (7)$$

374 Finally, among the 39 snowpits available for evaluation on February 21, only 15 pits in open areas
 375 (i.e. grasslands) were retained for evaluation and snow pits without SnowSAR measurements
 376 within a radius of 100 m were discarded.

377

378 5. Results and Discussion

379 5.1. Successful Retrievals

380 SnowSAR measurements are strongly affected by aircraft operations, viewing geometry that varies
 381 systematically along the flight path resulting in amplitude artifacts amplified by landform and
 382 landcover heterogeneity. Even after separating homogeneous grassland pixels, there is
 383 contamination from multiple bounce artifacts at grassland-forest transitions and adjacent wetlands
 384 that cannot be resolved at 30 or 90 m resolution. Other errors embedded in the retrieval are
 385 associated with downscaling of HRRR forcings that produce biased snow priors, snow hydrology
 386 model structure, and errors tied to the background backscatter estimation. Combined these errors
 387 compounded can lead to a weak convergence of the Bayesian optimization algorithm resulting in
 388 large backscatter residuals. To account for these errors and meet NASEM (2018) science
 389 requirements, SnowSAR pixels for which the relative residual backscatter (RRB) between Base-
 390 AM simulated σ_{sim}^{tot} and SnowSAR measurements σ_{SAR}^{tot} was greater than 30% were identified as
 391 unsuccessful. In an operational context, these pixels would be flagged and identified as failed or
 392 highly uncertain retrievals. The successful retrieval fraction after restricting the range of incidence
 393 angles and imposing the $RRB < 30\%$ criterion is summarized in Table 4 for the four flights, and
 394 for both 1|2 layer snowpack retrievals at 30 and 90 m resolution. Except for the later flight path
 395 over the predominantly forested areas in the eastern sector of Grand Mesa (Fig.1), the fraction of
 396 successful retrievals by restricting the incidence angle and RRB varies between 75 and 87% across
 397 the four SnowSAR flights with a maximum absolute bias of 1.2 dB. Only figures with retrieval
 398 results at 30 m resolution are shown in the main text; retrieval results at 90 m resolution as well as
 399 other supporting analysis can be found in Appendix A.

400

401 **Table 4:** Spatial bias between SnowSAR backscatter and converged backscatter from Base-AM for successful retrievals for
 402 grassland pixels at 30 and 90 m spatial resolution over each flight. Successful retrievals are for pixels with local incidence angles

403 in the 30°-45° range and relative residual backscatter (RRB) of less than 30% for each of the four flights. Shaded columns are for
 404 retrievals at 90 m resolution.

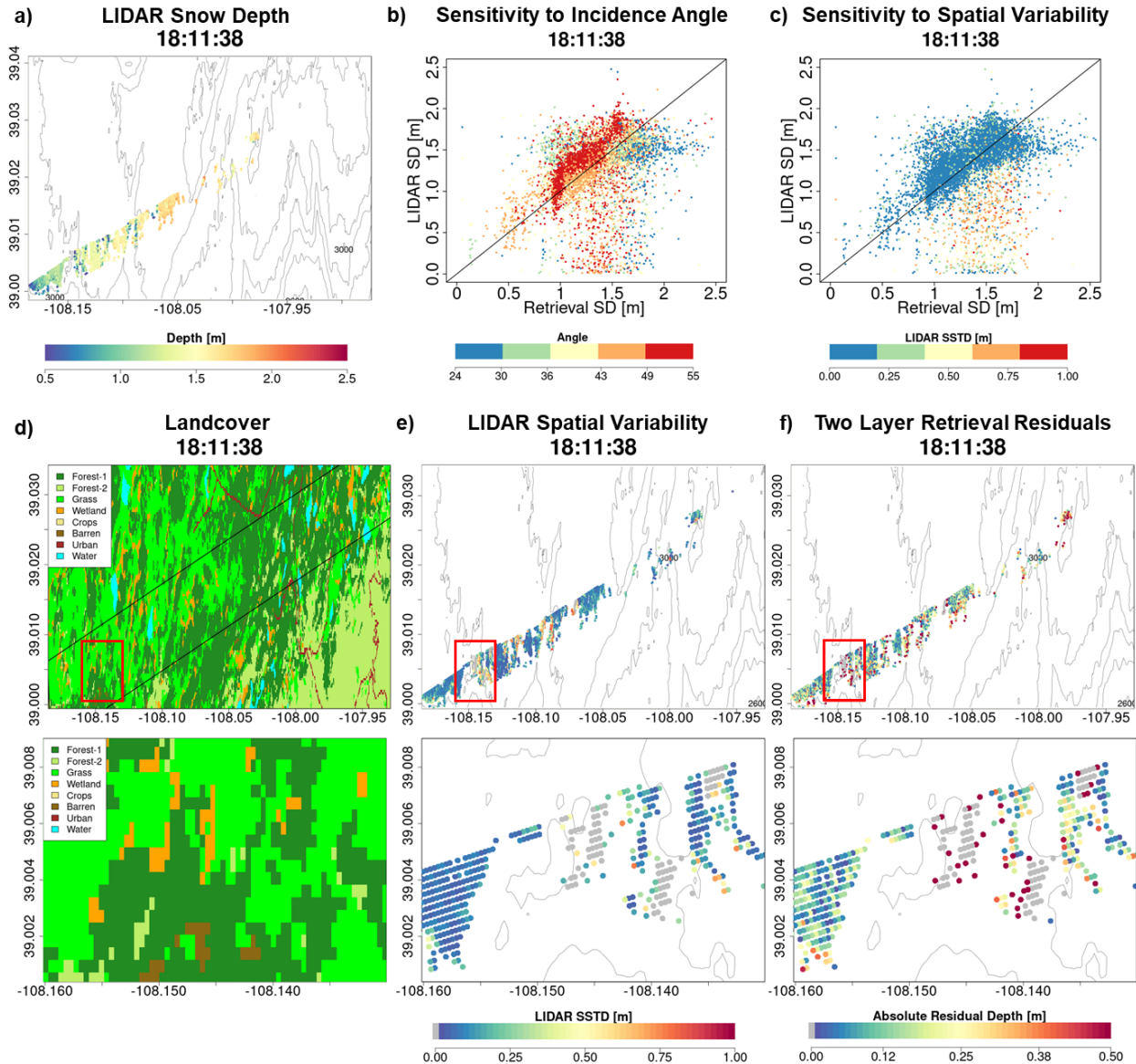
Flight Time	Successful Retrieval Fraction				Bias (Observed - Converged) [dB]							
	1 Layer		2 Layer		1 Layer				2 Layer			
	30 m	90 m	30 m	90 m	30 m		90 m		30 m		90 m	
					X	Ku	X	Ku	X	Ku	X	Ku
18:11:38	0.86	0.87	0.85	0.86	0.92	-0.45	0.96	-0.48	0.94	-0.46	0.97	-0.50
18:43:20	0.75	0.75	0.75	0.75	1.08	-0.54	0.98	-0.36	1.07	-0.46	0.98	-0.37
18:59:02	0.78	0.81	0.81	0.81	1.20	-0.78	1.21	-0.79	1.15	-0.73	1.22	-0.83
20:23:38	0.66	0.69	0.57	0.69	0.51	-0.58	0.70	-0.43	0.62	-0.85	0.72	-0.45

405

406 5.2. Retrieval Skill

407 Figure 7 compares LIDAR snow depth (Fig. 7a) against colocated SnowSAR retrievals at 30 m
 408 for the SNOWSAR flight at 18:11:38 GMT(GMT=MST+6). The SnowSAR retrievals for high
 409 incidence angles underestimate the LIDAR snow depth (orange and red points). Lemmetyinen et
 410 al. (2022) suggested a nominal incidence angle of 35°-45° for retrievals ensuring proper focusing
 411 and calibration of SnowSAR swaths. CB23 showed good skill in forward backscatter simulations
 412 for incidence angles as low as 30°. Overall the retrievals here also show very good performance
 413 for incidence angles between 30°-45°. Note however the large residuals for SnowSAR retrievals
 414 with high incidence angles (red and orange points in Fig. 7b) corresponding to LIDAR pixels with
 415 shallow snow depth (below the 1:1 line) and large subgrid-scale variability (orange and red points,
 416 Fig. 7c). Analysis for all flights at both 30 and 90 m resolution can be found in Appendix A (
 417 please see Figs. A1 and A2 similar to Fig. 7b; and Figs. A3 and A4 similar to Fig. 7c). Figures
 418 7d, 7e, and 7f show the landcover, spatial distribution of subgrid standard deviation (SSTD) and
 419 absolute residual (Retrieved – LIDAR) snow depth for the same flight. Along the edges of forest,
 420 the SSTD in the upscaled pixels is large due to high heterogeneity that cannot be resolved by the
 421 the LIDAR fusion algorithm for snow depth retrieval (Painter et al. 2016). The red box identifies
 422 an area with complex grassland-forest boundaries (Fig. 7d) and high subgrid scale variability (Fig.
 423 7e) resulting in poor LIDAR estimates. The edge of wetlands also has comparatively higher
 424 residuals than completely homogeneous grasslands. This corresponds to the LIDAR pixels with
 425 SSTD > 0.3 m (yellow, orange and red in Fig. 7c). Therefore, only LIDAR pixels with SSTD ≤
 426 0.3m are used for assessment of retrievals.

427



428

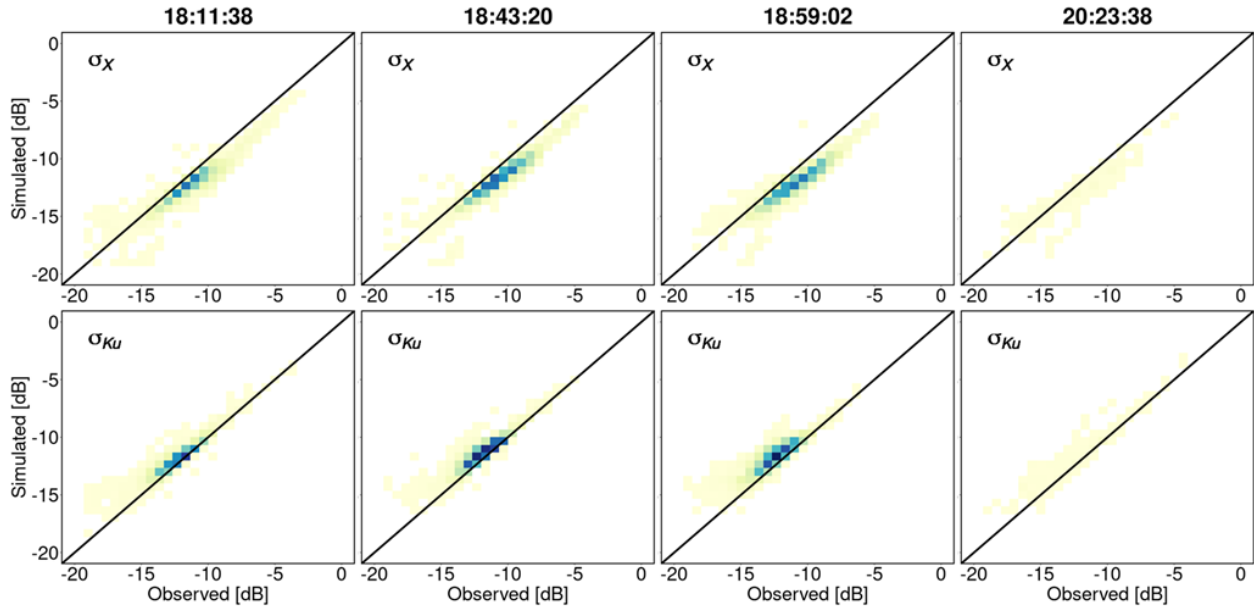
429 **Figure 7:** Snow depth measurements using airborne LIDAR on 2/25/17, 4 days after the SnowSAR flights. b) Comparison between
 430 LIDAR snow depth and the 2-layer retrieved snow depth from SnowSAR on 2/21/17 at 18:11:38 GMT. The pixels are color-coded
 431 according to the SnowSAR incidence angle. c) same as (b) with pixels color-coded according to the subgrid-scale variability
 432 measured by standard deviation of LIDAR snow depth within the corresponding 30 m pixel. Pixels on the edge of forests and
 433 grasslands have higher subgridscale standard deviations (SSTD). d) Landcover distribution along the flight path; bottom panel –
 434 zoom view of area in red box. e) Spatial distribution of upscaled LIDAR snow depth SSTD at 30m; bottom panel – zoom view of
 435 area in red box. The edges of forests have higher SSTD due to errors in the LIDAR snow depth retrievals at high resolution. f)
 436 Absolute residual between retrievals and LIDAR snow depth; bottom panel – zoom view of area in red box. Residuals equal to 0.5
 437 m and above are grouped in the same category. The red box in parts (d), (e), and (f) delineates an area with large absolute residuals.
 438 Vegetation-snowpack backscatter interactions at the grassland-forest and grassland-wetland margins not accounted for in the
 439 retrievals. Gray points in the central panel correspond to zero depth LIDAR estimates due to errors in heterogenous landcover.

440 Figure 8 shows heatmaps (density maps) to compare successful retrievals against observed X- and
 441 Ku-band VV-pol total backscatter at 30 m resolution. There is good agreement between the two
 442 values for both the bands specially in the -15 to -10 dB range without significant differences
 443 between single and two-layer snowpack retrievals. Note the positive bias in the case of X-band

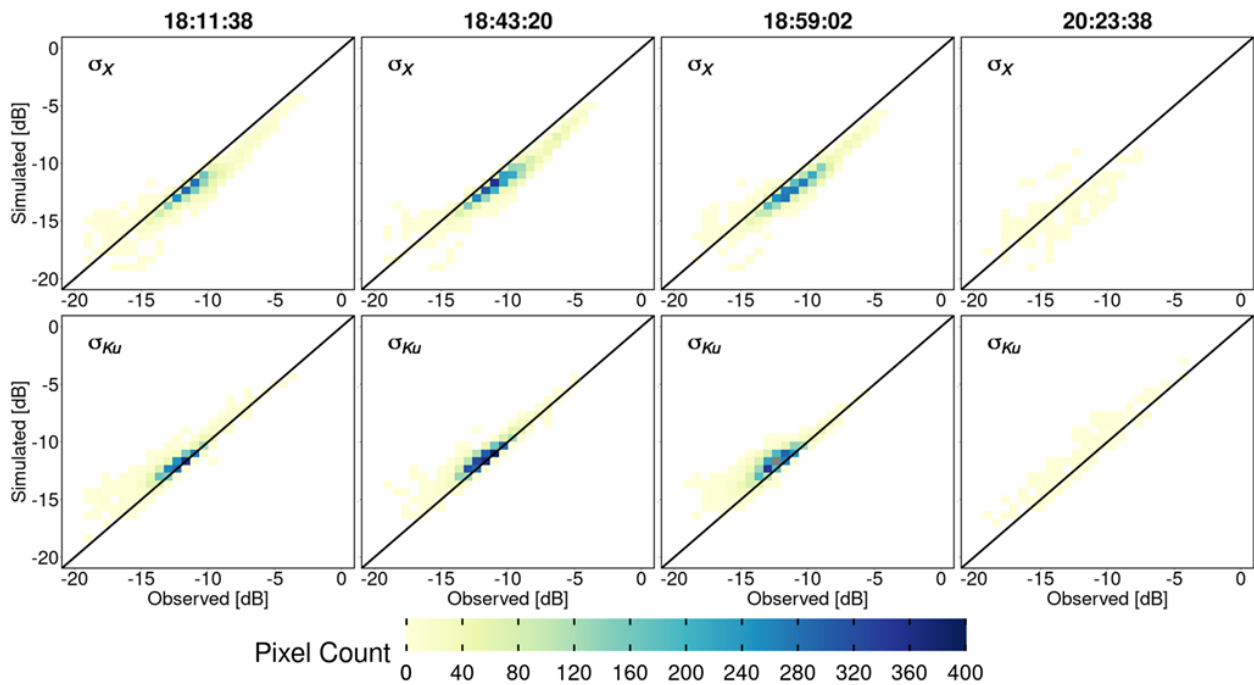
444 simulations compared to observations, whereas Ku-band has a negative bias as quantified in Table
 445 4. Overall, the retrievals at 90 m resolution show better agreement than those at 30 m resolution
 446 due to averaging (Fig. A5).

447

a) Single-Layer Retrievals



b) Two-Layer Retrievals



448

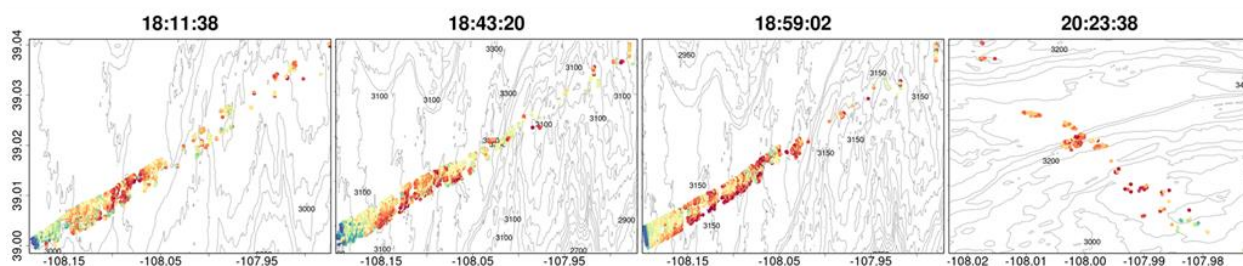
449 **Figure 8:** Heatmaps of SnowSAR measurements (observed) versus retrievals (simulated) backscatter (σ) at 30 m resolution for X-
 450 (σ_X) and Ku- (σ_{Ku}) bands: a) single-layer snowpack; and b) 2-layer snowpack. Successful retrievals are for pixels with local

451 incidence angles in the 30°- 45° range and relative residual backscatter (RRB) of less than 30% for each of the four flights (see
452 Table 4).

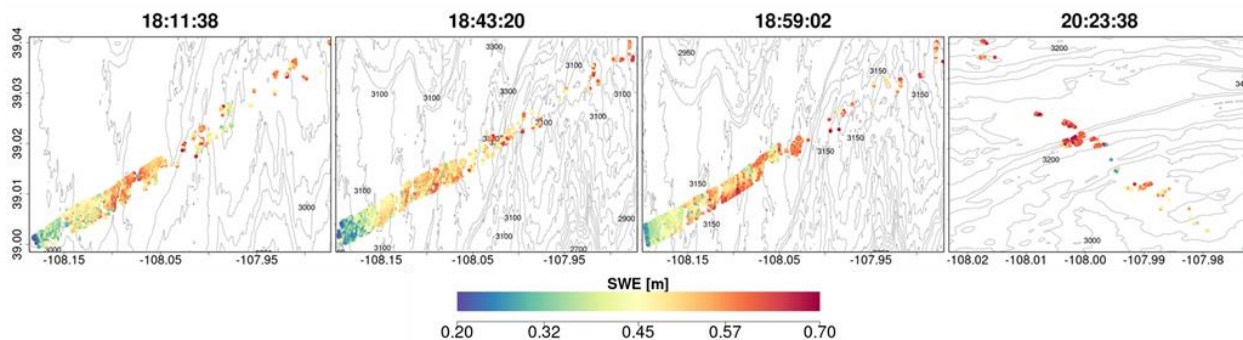
453
454 Maps of successful SWE retrievals for the four SnowSAR flight paths are shown in Fig. 9 and
455 Fig. A6 at 30 m and 90 m resolution, respectively. The retrievals capture well the west-east
456 gradient in SWE, and show realistic spatial variability across Grand Mesa. The very low SWE and
457 shallower snow depths at the easternmost boundary of the flightlines are underestimates
458 introduced by upscaling of the SNOWSAR backscatter values where there are significant changes
459 in topography at the edge of the Plateau (see Fig.2).

460

a) Single-Layer SWE Retrievals



b) Two-Layer SWE Retrievals

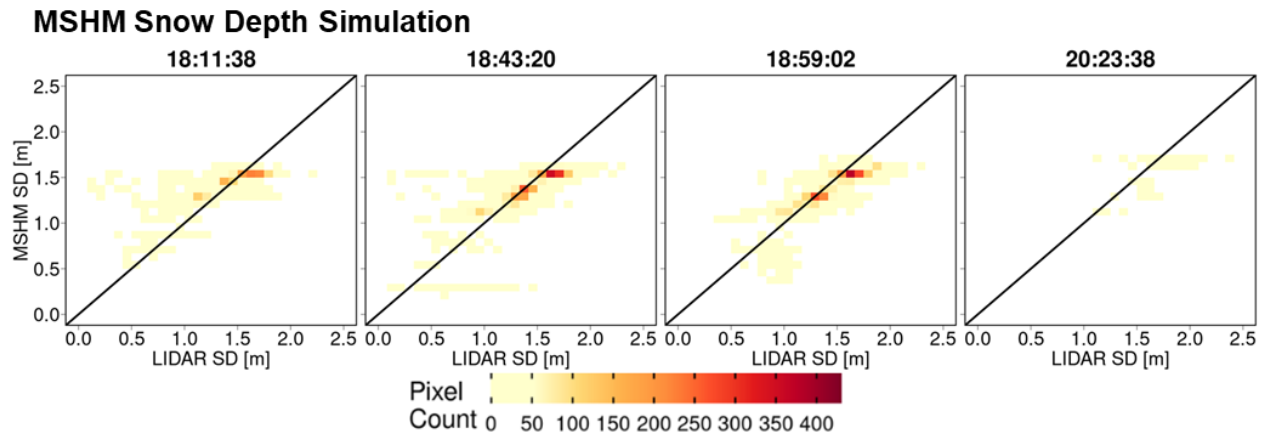


461
462 **Figure 9:** Spatial distribution of successful SWE retrievals for 1-layer (a) and 2-layer (b) snowpacks in grassland pixels at 30 m
463 resolution. Successful retrievals are for pixels with local incidence angles in the 30°- 45° range and relative residual backscatter
464 (RRB) of less than 30% for each of the four flights (see Table 4).

465
466 Heatmaps of total snow depth priors (MSHM predicted snow depth) against LIDAR snow depth
467 are shown in Fig. 10 and Figs. A7 at 30 m and 90 m resolution and can be contrasted with heatmaps
468 of total snow depth posteriors) against LIDAR snow depth in Figs. 11 and A8 using both single
469 and two-layer retrievals. Note the narrow range of the prior snow depths concentrated around 1.5
470 m and the positive bias relative to LIDAR. The posteriors show much wider range of variability
471 and deeper snow consistent with the LIDAR data for both single and two-layer retrievals, albeit
472 with better agreement for the latter with high counts overlaying the 1:1 line at both spatial

473 resolutions. This behavior is further confirmed by examining the snow depth histograms in Figs.
 474 A9 and A10. The retrievals capture well the range of the LIDAR snow depths for all flights, and
 475 there is a substantial improvement in the shape of the distributions as revealed by the heatmaps.

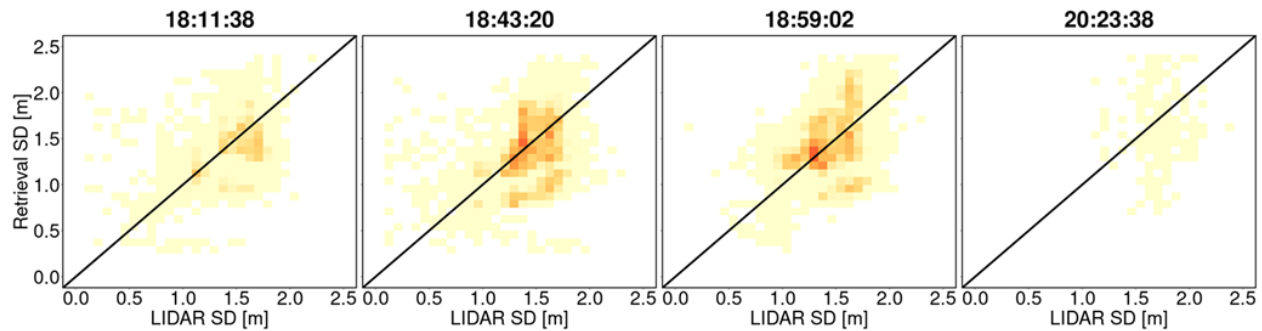
476



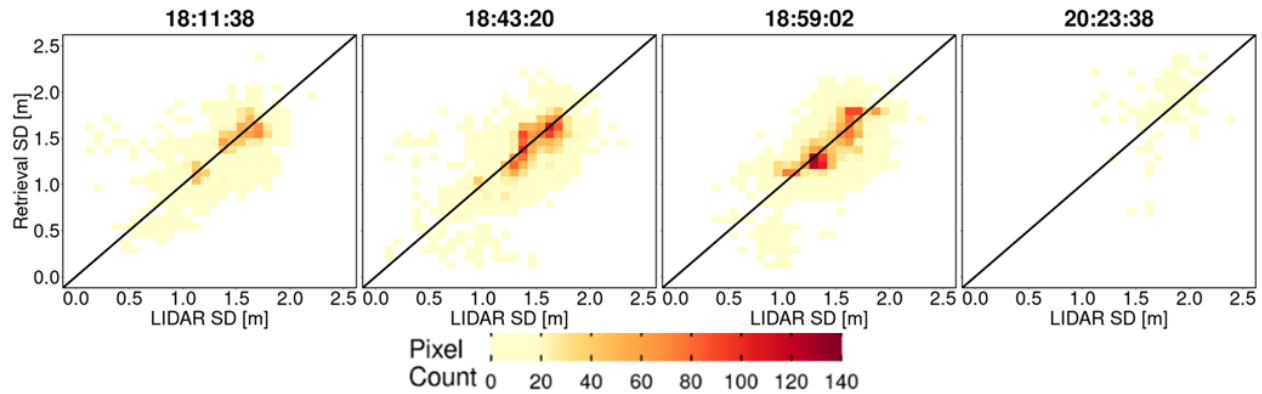
477

478 **Figure 10:** Heatmap of LIDAR and MSHM predicted snow depth priors at 30 m resolution using overlapping pixels from the
 479 MSHM and LIDAR. Only pixels with incidence angle between 30° - 45° , and moderate sub-grid scale variability of LIDAR snow
 480 depth (< 0.3).

a) Single-Layer Snow Depth Retrievals



b) Two-Layer Snow Depth Retrievals



481

482 **Figure 11:** Heatmap of LIDAR versus successful snow depth (SD) retrievals at 30 m resolution using overlapping LIDAR and
 483 retrieval pixels. Successful retrievals are for pixels with local SnowSAR incidence angles in the 30°- 45° range and relative residual
 484 backscatter (RRB) of less than 30% for each of the four flights (see Table 4). LIDAR SD in pixels with subgrid scale variability
 485 corresponding to standard deviation of less than 0.3 m for the upscaled 90 m LIDAR pixel are not included.

486

487 Quantitative assessment metrics are presented in Tables 5 and A1 for the comparison between
 488 various snow depth datasets at 30 and 90 m resolutions, respectively. The snow depth MARE is
 489 higher for the retrievals compared to the priors (MSHM) due to the fact that MARE is an effective
 490 metric capturing distance from the mean. CB20 showed that the MSHM simulated average snow
 491 mass accumulation at the Grand Mesa scale is within 10% of observations at a monthly time-scale
 492 in February 2017. The BC coefficients The BC coefficients of 0.95 and above at 30 m resolution
 493 indicate significant agreement between the shapes of the distributions at 0.95 or above at 30m
 494 resolution using the two-layer retrievals for the west-east flights, and 0.76 for the fourth flight at
 495 20:23:38 GMT over the forested area. There is significant improvement relative to MSHM priors
 496 in the statistical similarity of the snow depth retrievals vis-à-vis the LIDAR data for all cases, and
 497 more so for the fourth flight over the forest. For snow depth, 30 m resolution and two-layer
 498 retrievals outperform the 90 m resolution and single-layer retrievals for all flights. This is
 499 explained in part by landcover classification errors that are smaller at 30 m. Figure A11 shows
 500 that the number of pixels where retrievals produce large mean absolute residuals is very small and
 501 characterize by low confidence in the LIDAR estimates.

502

503 **Table 5:** Summary of statistics and error metrics of the 3 snow depth (SD) data sets at 30 m resolution: LIDAR measurements,
 504 MSHM predictions, and successful SnowSAR retrievals for grassland pixels and subgrid-scale standard deviation (σ) of less than
 505 0.3 m for the upscaled LIDAR pixel. MARE – Mean Absolute Relative Error (Eq. 6); BC – Bhattacharya Coefficient (Eq. 7). Here
 506 mean and standard deviation refer to the spatial distribution, unlike the prior mean and standard deviation used in Base-AM (Table
 507 3). Successful retrievals are for pixels with local incidence angles in the 30°- 45° range and relative residual backscatter (RRB) of
 508 less than 30% for each of the four flights (see Table 4).

Flight (GMT)	N Layer	Spatial SD μ [m]			Spatial SD σ [m]			MARE SD		BC SD	
		Retrieved	MSHM	LIDAR	Retrieved	MSHM	LIDAR	Retrieved-LIDAR	MSHM-LIDAR	Retrieved-LIDAR	MSHM-LIDAR
18:11:38	1	1.39	1.42	1.42	0.32	0.15	0.28	0.19	0.11	0.94	0.67
18:43:20		1.41	1.38	1.42	0.32	0.21	0.27	0.18	0.11	0.96	0.75
18:59:02		1.49	1.38	1.44	0.33	0.20	0.27	0.18	0.09	0.94	0.76
20:23:38		1.66	1.58	1.77	0.36	0.16	0.22	0.21	0.13	0.71	0.25
18:11:38	2	1.38	1.41	1.40	0.30	0.17	0.29	0.14	0.12	0.98	0.67
18:43:20		1.35	1.38	1.42	0.31	0.20	0.28	0.14	0.11	0.97	0.75
18:59:02		1.40	1.38	1.44	0.31	0.20	0.27	0.12	0.09	0.95	0.75
20:23:38		1.89	1.61	1.80	0.39	0.14	0.24	0.17	0.12	0.76	0.23

509

510 Tables 6 and A2 summarize the average absolute relative errors between snowpits and SWE
 511 retrievals from all flights within 100 m of the snowpits. The results are significantly better for two-
 512 layer snowpack retrievals. The mean absolute relative errors at 30 m resolution are 0.22 and 0.13
 513 for 1 layer and 2 layer snowpacks respectively. The mean absolute relative errors at 90 m resolution

514 are 0.2 and 0.12 for 1 layer and 2 layer snowpacks respectively. There is a variable number of
 515 pixels used for the calculation of the error metrics for each snow pit, which in the case of 51S is
 516 so small that it suggests the pit is not in the flight path. The large errors for pits 4500, 44E and and
 517 53W are attributed to very heterogeneous landcover including water and forest (4500), and
 518 proximity to roads (53W and 44E). After removing these snowpits in the central area marked in
 519 Fig. A12, the average absolute relative SWE residuals are 5-7% (15-18%) for the two-layer (single-
 520 layer) retrieval algorithm.

521

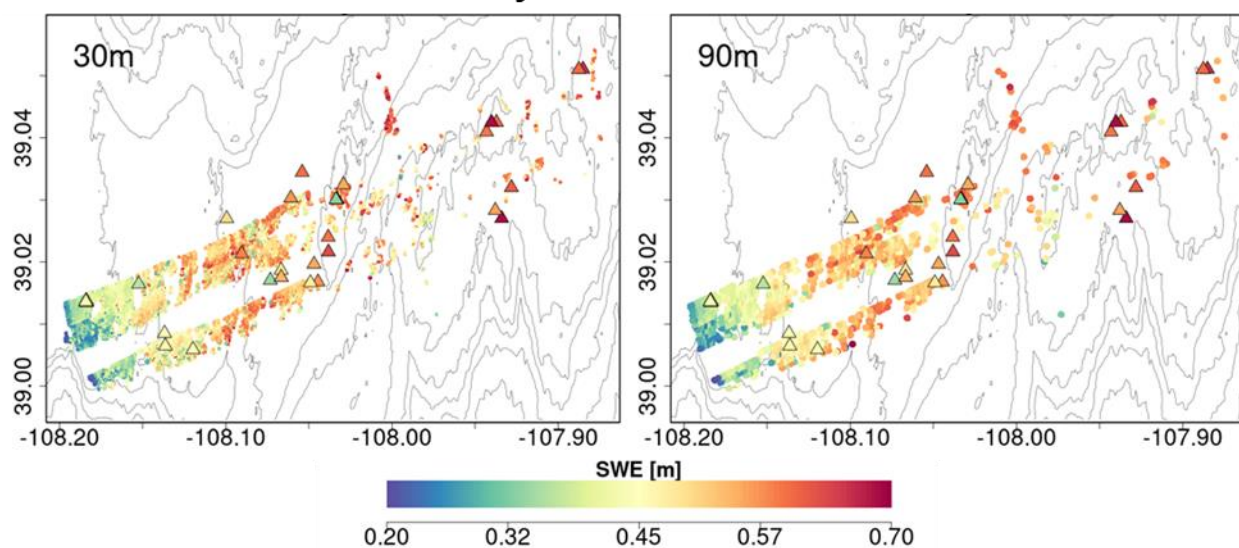
522 **Table 6:** Evaluation of successful SWE retrievals at 30 m resolution against SWE at SnowEx'17 snow pits and
 523 retrieved snowpacks at 30 m resolution. All N pixels with centroids within 100 m of each snow pit are in the Grasslands
 524 (according to the Landcover dataset at 30 m resolution, see Table 1). SD – snow depth. Italicized rows correspond to
 525 large local MARE (Mean Absolute Relative Error, Eq. 6).

Date	x	y	Pit SD (m)	Pit SWE (m)	Retrieved SWE (m)		MARE		N pixels	Avg. Dist (m)	Pit ID
					1 Lyr	2 Lyr	1 Lyr	2 Lyr			
2/20/2017	-108.184	39.014	1.15	0.368	0.455	0.386	0.236	0.049	28	18	KC1C
2/20/2017	-108.184	39.014	1.19	0.386	0.457	0.387	0.184	0.003	27	12	KC1E
2/20/2017	-108.184	39.014	1.18	0.386	0.456	0.387	0.181	0.003	26	15	KC1N
2/20/2017	-108.184	39.013	1.24	0.414	0.456	0.387	0.101	0.065	27	20	KC1S
2/20/2017	-108.184	39.014	1.30	0.435	0.455	0.385	0.046	0.115	29	11	KC1W
2/22/2017	-108.136	39.006	1.32	0.436	0.556	0.484	0.275	0.110	22	8	29E
2/22/2017	-108.090	39.021	1.65	0.583	0.685	0.596	0.175	0.022	19	17	38E
2/22/2017	<i>-108.060</i>	<i>39.030</i>	<i>2.10</i>	<i>0.763</i>	<i>0.368</i>	<i>0.449</i>	<i>0.518</i>	<i>0.412</i>	<i>12</i>	<i>16</i>	<i>53W</i>
2/22/2017	-108.044	39.017	1.68	0.566	0.480	0.505	0.152	0.108	5	51	63E
2/22/2017	-108.049	39.017	1.49	0.48	0.494	0.513	0.029	0.069	13	29	63W
2/22/2017	-108.029	39.032	1.66	0.55	0.558	0.581	0.015	0.056	18	15	67N
2/23/2017	<i>-108.067</i>	<i>39.029</i>	<i>2.13</i>	<i>0.761</i>	<i>0.593</i>	<i>0.504</i>	<i>0.221</i>	<i>0.338</i>	<i>9</i>	<i>23</i>	<i>44E</i>
2/23/2017	<i>-108.061</i>	<i>39.030</i>	<i>1.59</i>	<i>0.568</i>	<i>0.365</i>	<i>0.408</i>	<i>0.357</i>	<i>0.282</i>	<i>3</i>	<i>75</i>	<i>51S</i>
2/24/2017	-108.033	39.030	1.80	0.576	0.657	0.573	0.141	0.005	20	10	0
2/24/2017	-108.033	39.030	1.84	0.598	0.652	0.581	0.090	0.028	21	14	800
2/24/2017	-108.033	39.030	1.80	0.571	0.650	0.581	0.138	0.018	22	19	1390
2/24/2017	-108.033	39.030	1.75	0.566	0.654	0.581	0.155	0.027	21	15	2000
2/24/2017	-108.033	39.030	1.67	0.560	0.654	0.581	0.168	0.037	21	9	2500
2/24/2017	<i>-108.034</i>	<i>39.030</i>	<i>1.12</i>	<i>0.331</i>	<i>0.660</i>	<i>0.580</i>	<i>0.994</i>	<i>0.752</i>	<i>18</i>	<i>19</i>	<i>4500</i>
Mean			1.56	0.52	0.54	0.50	0.22	0.13	19.00	20.84	

526

527 Finally, composite spatial maps of successful SWE retrievals from all flights overlain by the
 528 snowpit measurements between 20-24 February are shown in Fig. 12. Because of the different
 529 viewing geometries, retrievals between incident angles 30°-35° for flight path at 18:59:02 in the
 530 composite of overlapping flight paths at 18:43:20 and 18:59:02 GMT were removed. Note the
 531 consistency at 30 m and 90 m resolutions as well as the overall agreement between SWE at
 532 snowpits and SWE retrievals on the flightlines.

Two-Layer SWE Retrievals



533

534 **Figure 12:** Composite spatial distribution of SWE (2-layer retrievals) successfully retrieved at 30m (left) and 90m (right) resolution
535 for grassland pixels for the four SnowSAR flights. Snow pits (20-24 Feb, Fig. 4, Tables 6) are marked by triangles colored according
536 to SWE. SnowEx'17 snow pit locations are marked by triangles and colored according to SWE. Successful retrievals are for pixels
537 with local incidence angles in the 30°- 45° range and relative residual backscatter (RRB) of less than 30% for each of the four
538 flights (see Table 4). As two flights Gray elevation contours are plotted every 100m.

539

540 6. Conclusion

541 A Bayesian physical-statistical SWE retrieval framework leveraging prior work (CB20, CB23,
542 P17, P23, Fig. 5) was applied to airborne X- and Ku-band measurements yielding robust results
543 from multiple SnowSAR flights over grassland and mixed grassland and forest in Grand Mesa,
544 Colorado. Prior distributions of snowpack parameters were obtained from a multilayer snow
545 hydrology model with atmospheric forcing derived from operational NWP forecasts and analysis
546 (CB20, CB23). In order to reconcile the number of independent measurements, physical
547 constraints, and reduce the number of snowpack parameters, snowpack stratigraphy was mapped
548 into single-layer and two-layer snowpacks and then Bayesian inference using Base-AM was
549 applied (P17, P23). The SnowSAR measurements were averaged to 30 and 90 m resolutions, and
550 retrievals were conducted independently for every measurement pixel along the flight lines.
551 Retrievals for measurements with convergence backscatter relative errors less than 30% (± 1.2 dB)
552 and for incidence angles in the 30°- 45° range were considered successful over grasslands,
553 corresponding to 75 -87% of all retrievals depending on the flight.

554 The retrievals, specifically the local means of the posterior distributions, were evaluated against
555 the spatial distribution of LIDAR snow depth estimates up to 2 m and against snowpit SWE
556 measurements up to 700 mm and snow depth up to 2.13 m. Since the LIDAR and snowpit
557 measurements were not concurrent with the SnowSAR flights, the assessment of retrieval skill was
558 conducted over a period of five days without snowfall or significant day-to-day weather changes.
559 The two-layer snowpack retrievals perform better overall capturing the observed spatial gradients

560 of snow depth, with SWE relative errors $\leq 7\%$ as compared with 18% for single-layer SWE
561 retrievals, and snow depth absolute retrieval residuals 10-20% depending on landcover
562 heterogeneity and measurement uncertainty. The statistical structure of retrieved snow depth is
563 similar to that estimated by LIDAR, which is indicative of the retrievals ability to capture snow
564 patterns and scaling behavior to support scientific process studies. For satellite-based monitoring
565 from space in the context of a future snow mission, time-series of measurements would be
566 available that should improve the estimates of the priors based on antecedent information. This is
567 not possible for one-time observations during field experiments such as SnowEx'17, and thus
568 improved results would be expected under realistic satellite-based applications. NWP forecasts
569 are available worldwide and therefore this retrieval framework can be applied to SAR
570 measurements anywhere.

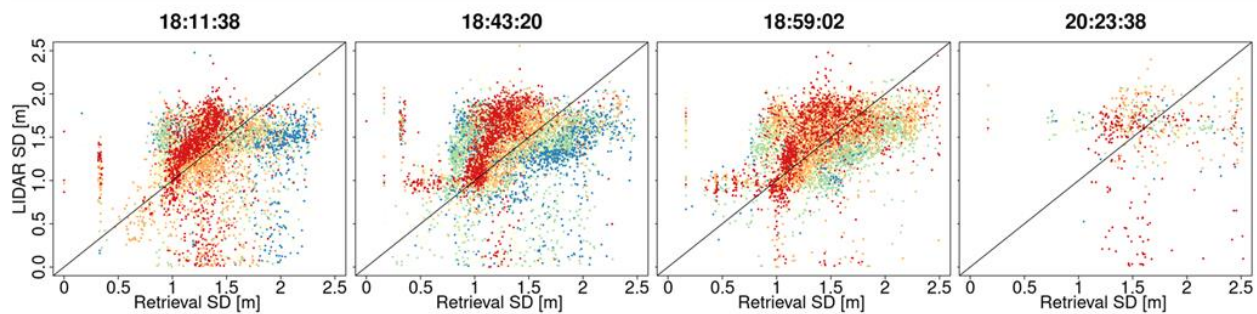
571 The radar model used in this study (MEMLS) does incorporate snow-ground-vegetation scattering
572 interactions. Grassland vegetation during the accumulation season is assumed to be submerged
573 and the impact of vegetation is included in the estimation of the background backscatter (σ_{bkg} , Fig.
574 1). Because the landcover data are categorical, in addition to the uncertainty of the data at 30 m
575 resolution, additional uncertainty is tied to the selection of homogeneous grassland pixels at 90
576 resolution, which explains some of the unsuccessful retrievals especially along the grassland-
577 forest, shrub and wetland boundaries. The potential for estimating σ_{bkg} independently for each
578 location as proposed by Cao and Barros (2023b) provides an alternative to simplify the retrieval
579 workflow and target the Bayesian inference to the snowmass and volume backscatter ($\sigma_{\text{vol}} = \sigma_{\text{total}} -$
580 σ_{bkg}).

581 Airborne measurements are characterized by large changes in viewing geometry across the flight-
582 line and due to other factors such as variable winds and turbulence depending on weather
583 conditions, thus pointing to improved skill from satellite platforms. Building on previous mission
584 concepts (e.g. Rott et al. 2012) and leveraging substantial theory advances and field campaigns in
585 the last decade, this study demonstrates the utility and effectiveness of X- and Ku-band SAR
586 technology to remotely monitor snowmass at high spatial resolution and with accuracy and
587 uncertainty that meet the requirements expressed in the most recent Earth Science and Applications
588 from Space Decadal Survey (NASEM, 2018).

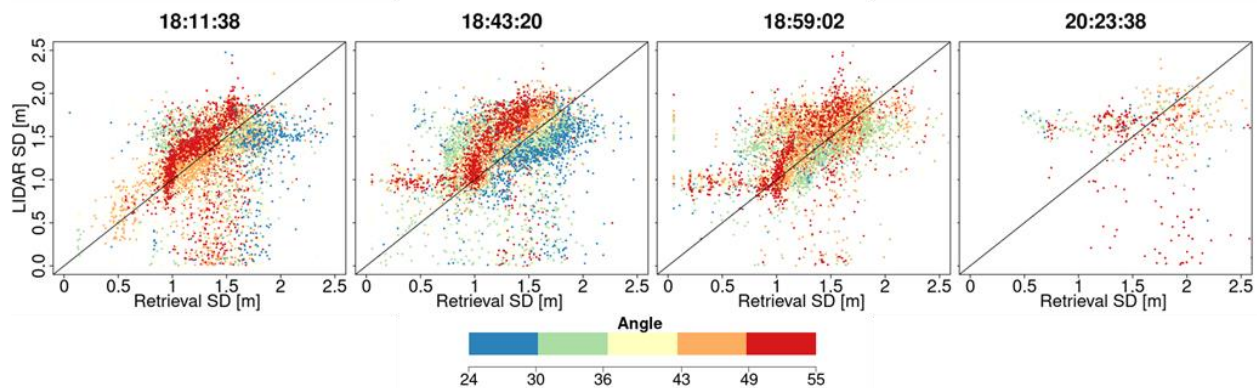
589
590
591
592
593
594
595
596

Sensitivity to Incidence Angle

a) Single-Layer Depth Retrieval



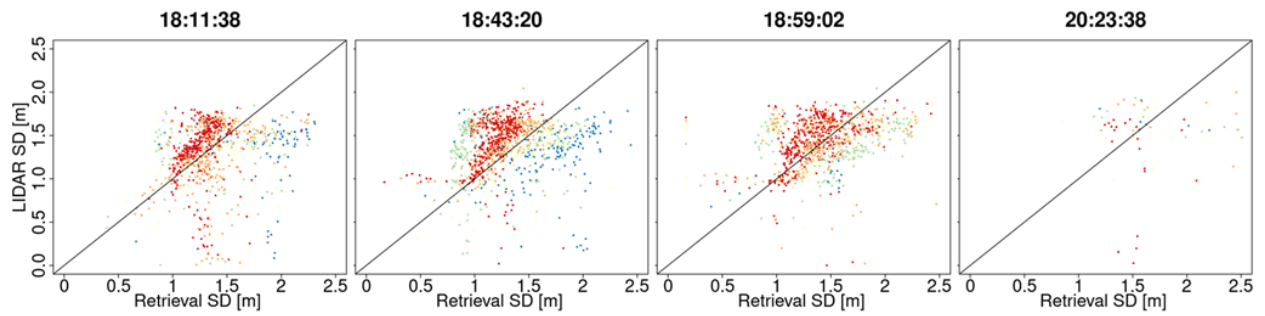
b) Two-Layer Depth Retrieval



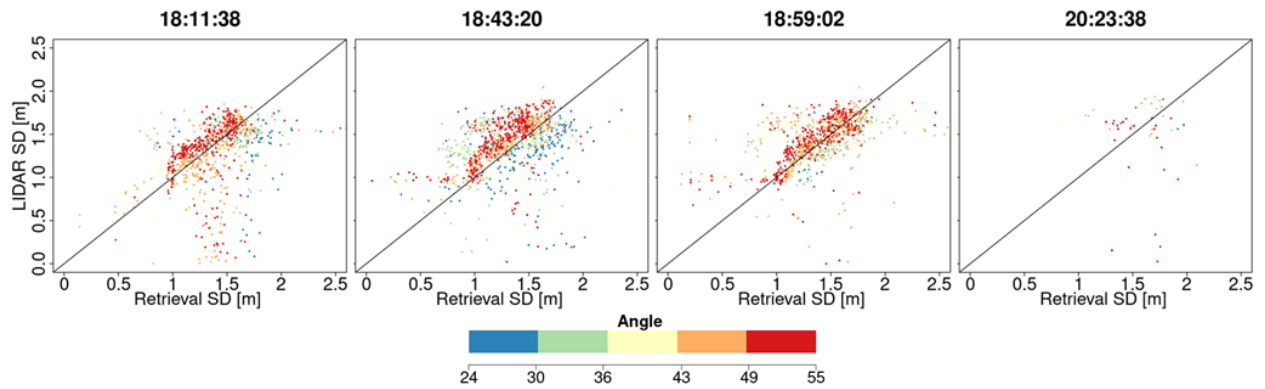
601 **Figure A1:** Same as Fig. 7b with pixels color coded according to the local SnowSAR incidence angle for all four flightlines and
602 for single-(top row) and two-layer (bottom row) retrievals at 30 m resolution.

Sensitivity to Incidence Angle

a) Single-Layer Depth Retrieval



b) Two-Layer Depth Retrieval



603

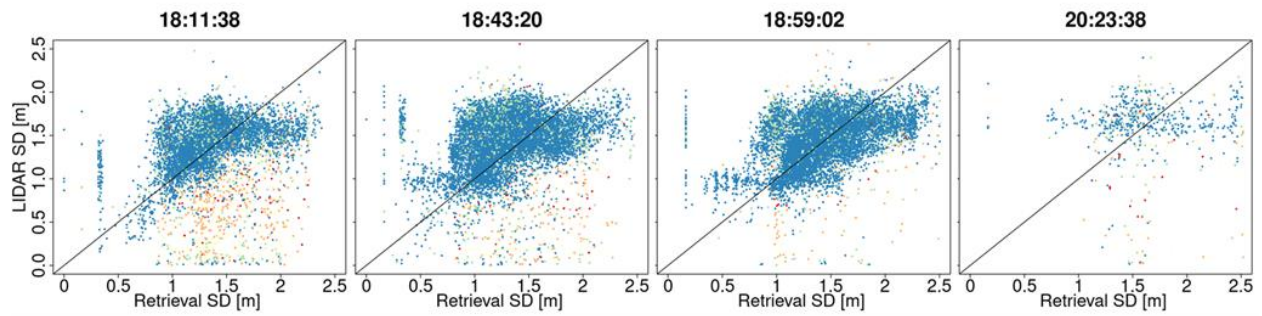
604 **Figure A2:** Same as Fig. 7b with pixels color coded according to the local SnowSAR incidence angle for all four flightlines and
605 for single-(top row) and two-layer (bottom row) retrievals at 90 m resolution.

606

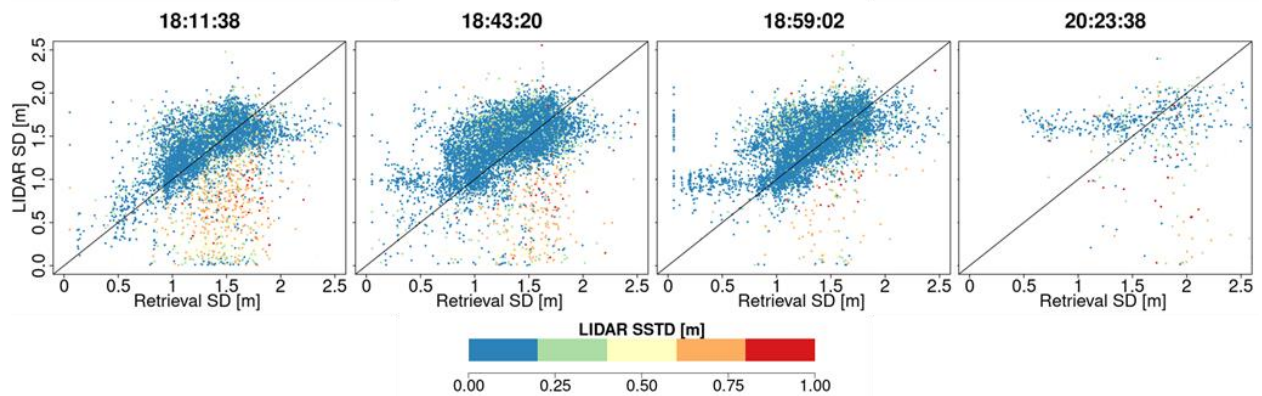
607

Sensitivity to Spatial Variability

a) Single-Layer Depth Retrieval



b) Two-Layer Depth Retrieval



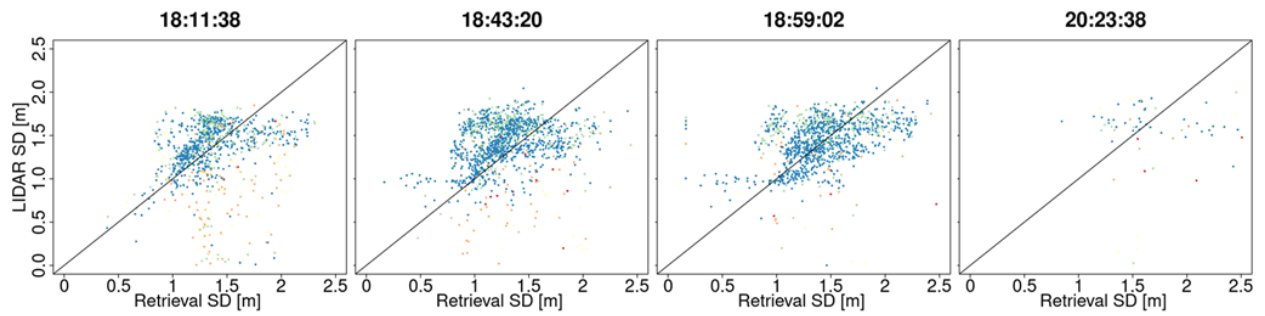
608

609 **Figure A3:** Comparison between LIDAR snow depth (SD) and successful retrievals for single and two-layer algorithms. The
610 pixels are color coded according to the subgrid scale variability of the 30 m upscaled LIDAR pixel.

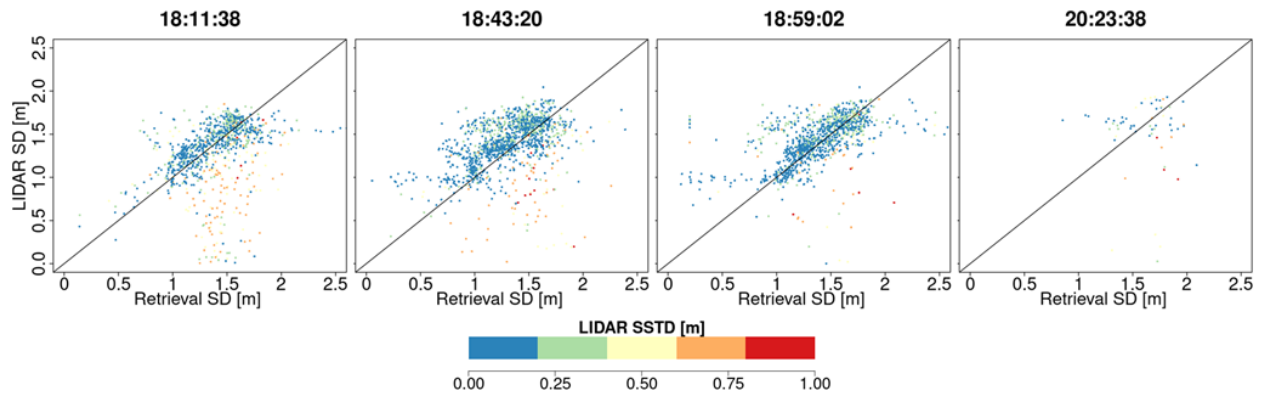
611

Sensitivity to Spatial Variability

a) Single-Layer Depth Retrieval



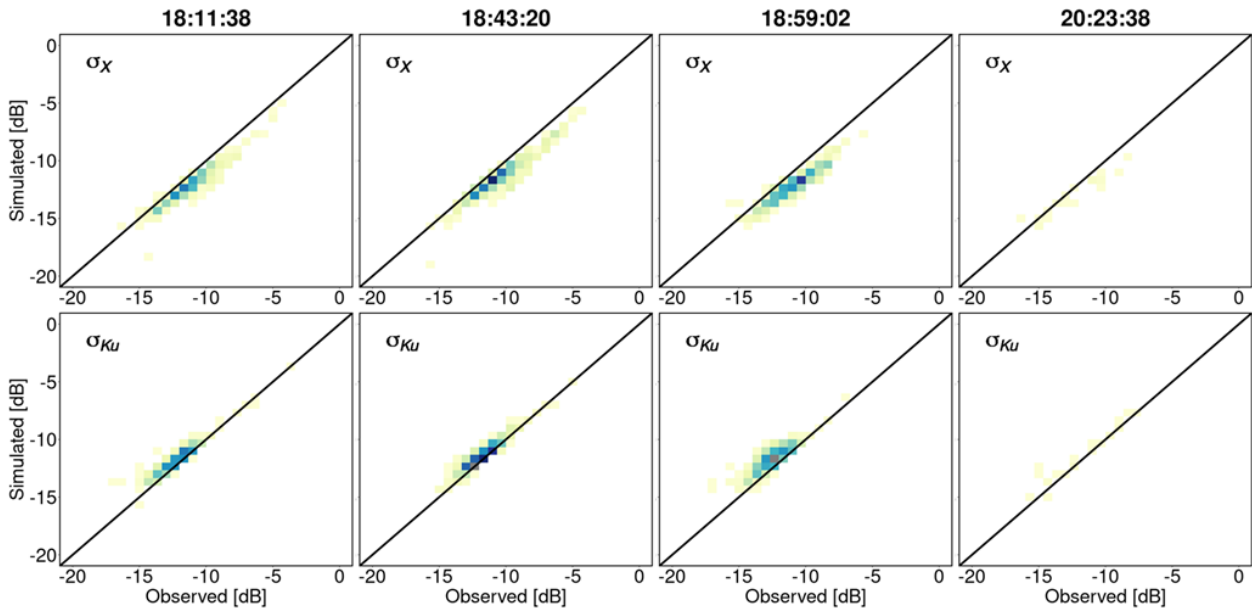
b) Two-Layer Depth Retrieval



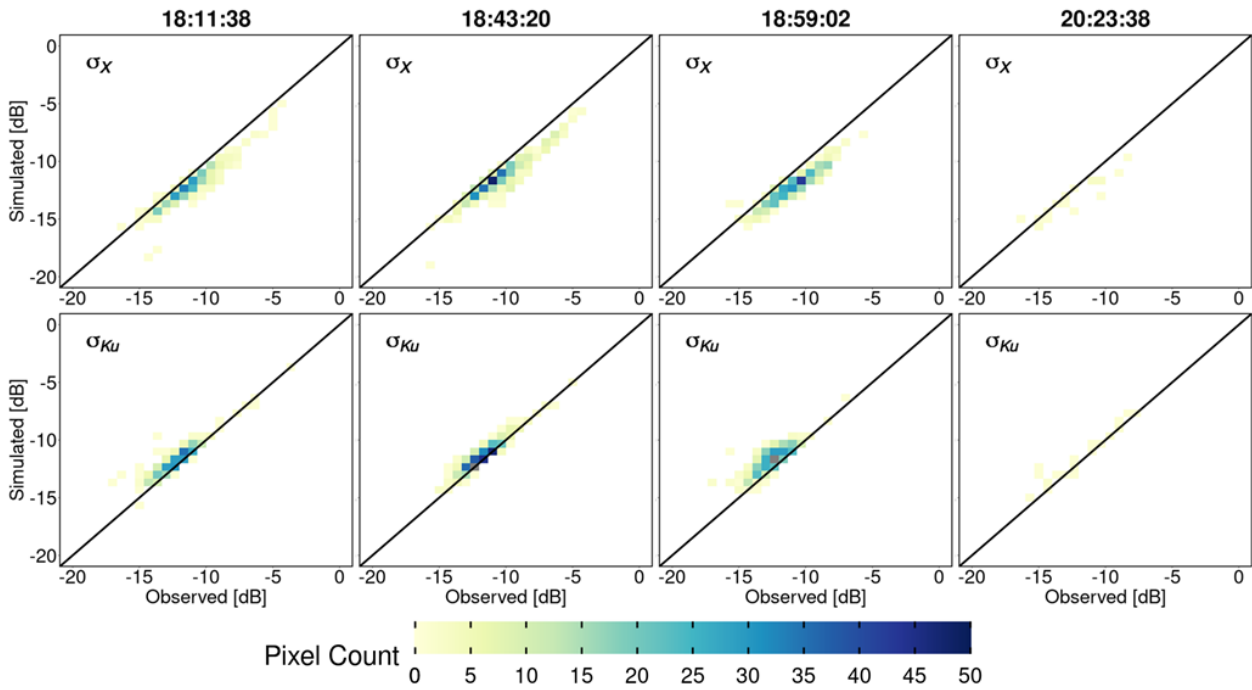
612

613 **Figure A4:** Comparison between SnowSAR snow depth and successful retrievals. The pixels are color coded according to the
614 subgrid scale variability of the 90 m upscaled LIDAR pixel.

a) Single-Layer Retrievals



b) Two-Layer Retrievals

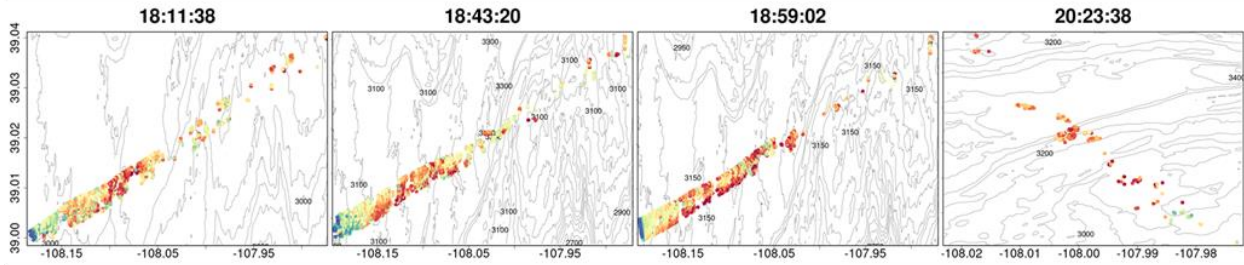


615

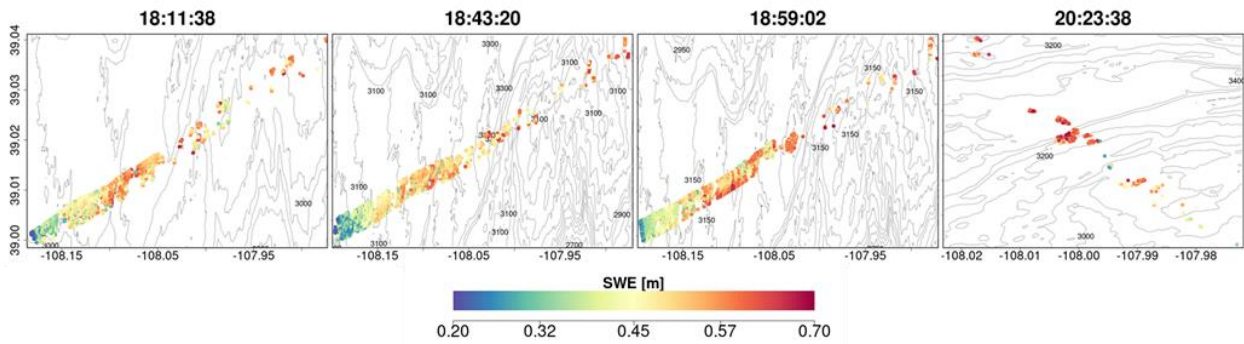
616 **Figure A5:** Heatmaps of SnowSAR backscatter measurements (observed) versus retrievals (simulated) backscatter at 90 m
 617 resolution: a) single-layer snowpack; b) 2-layer snowpack for X- (σ_X) and Ku- (σ_{Ku}) bands. Successful retrievals are for pixels
 618 with local incidence angles in the 30°- 45° range and relative residual backscatter (RRB) of less than 30% for each of the four
 619 flights (see Table 4).

620

a) Single-Layer SWE Retrievals



b) Two-Layer SWE Retrievals

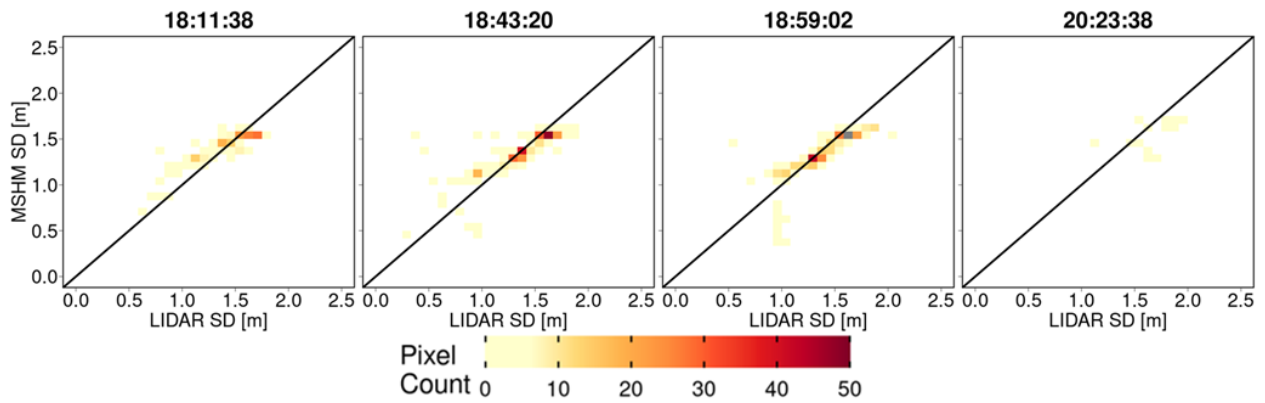


621

622 **Figure A6** Spatial distribution of successful SWE retrievals for 1-layer (a) and 2-layer (b) snowpacks in grassland pixels at 90 m
 623 resolution. Successful retrievals are for pixels with local incidence angles in the 30°- 45° range and relative residual backscatter
 624 (RRB) of less than 30% for each of the four flights (see Table 4).

625

MSHM Snow Depth Simulation

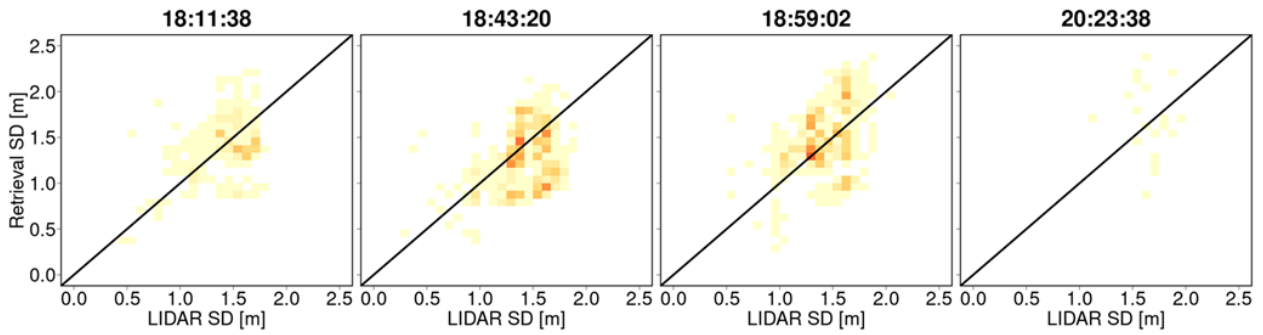


626

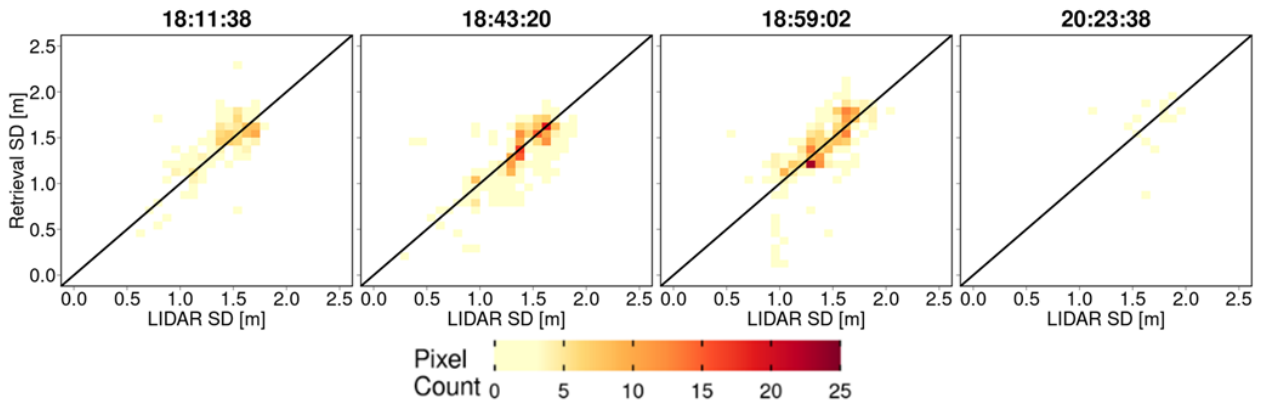
627 **Figure A7:** Heatmaps of LIDAR snow depth and snow depth predicted by MSHM at the time of SnowSAR flights for
 628 overlapping pixels at 90 m resolution.

629

a) Single-Layer Snow Depth Retrievals



b) Two-Layer Snow Depth Retrievals



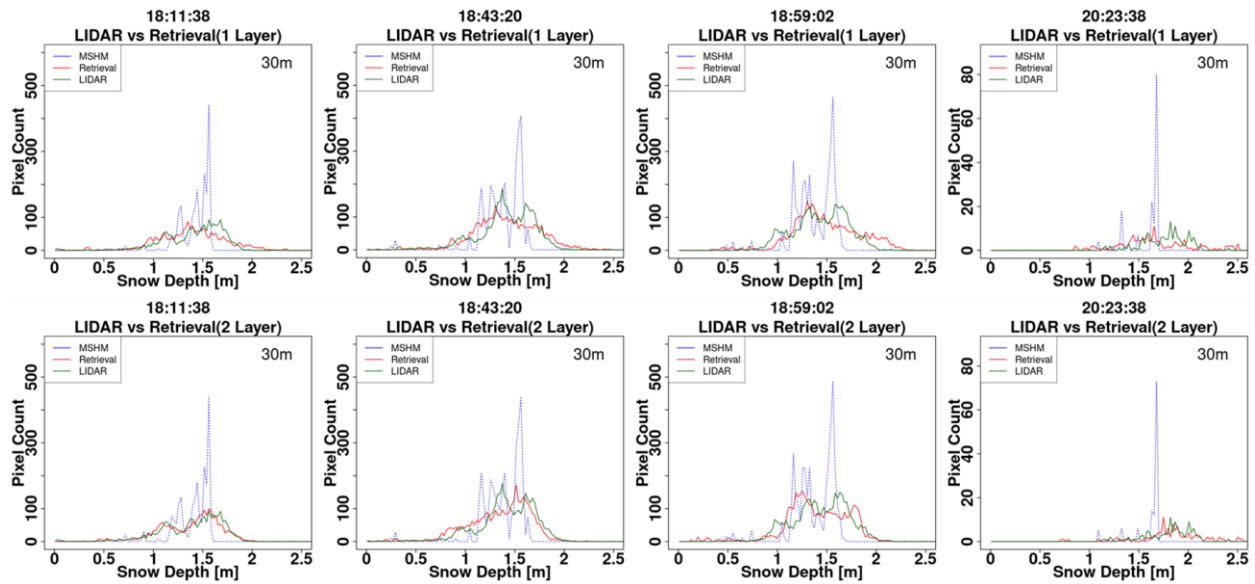
630

631 **Figure A8:** Heatmaps of LIDAR versus successful snow depth (SD) retrievals at 90 m resolution using overlapping LIDAR and
632 retrieval pixels. Successful retrievals are for pixels with local SnowSAR incidence angles in the 30°- 45° range and relative residual
633 backscatter (RRB) of less than 30% for each of the four flights (see Table 4). LIDAR SD in pixels with subgrid scale variability
634 corresponding to standard deviation of less than 0.3 m for the upscaled 90 m LIDAR pixel are not included.

635

636

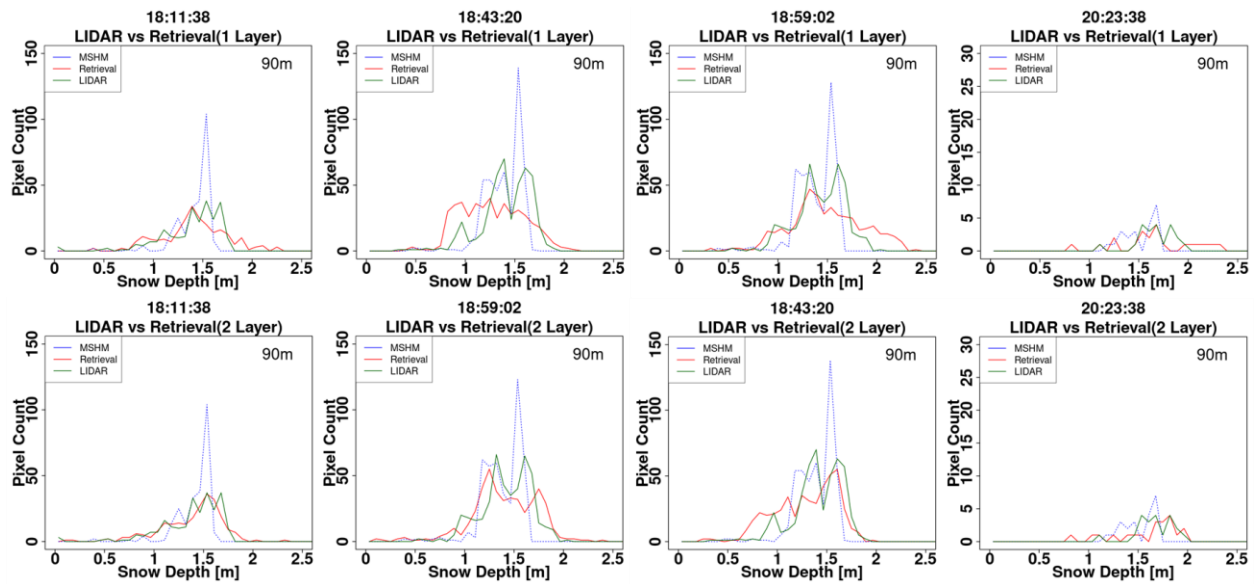
637



638

639 **Figure A9:** Histogram of snow depth (SD) from LIDAR, MSHM, and successful retrievals at 30 m using 1- and 2- layer
 640 snowpacks. The total number of pixels for each snow depth product is the same. Successful retrievals are for pixels with local
 641 incidence angles in the 30°- 45° range and relative residual backscatter (RRB) of less than 30% for each of the four flights (see
 642 Table 4). LIDAR SD in pixels with subgrid scale variability corresponding to standard deviation of less than 0.3 m for the
 643 upscaled 90 m LIDAR pixel are not included.

644



645

646 **Figure A10 -** Histogram of snow depth (SD) from LIDAR, MSHM, and successful retrievals at 90 m using 1- and 2- layer
 647 snowpacks. The total number of pixels for each snow depth product is the same. Successful retrievals are for pixels with local
 648 incidence angles in the 30°- 45° range and relative residual backscatter (RRB) of less than 30% for each of the four flights (see
 649 Table 4). LIDAR SD in pixels with subgrid scale variability corresponding to standard deviation of less than 0.3 m for the
 650 upscaled 90 m LIDAR pixel are not included.

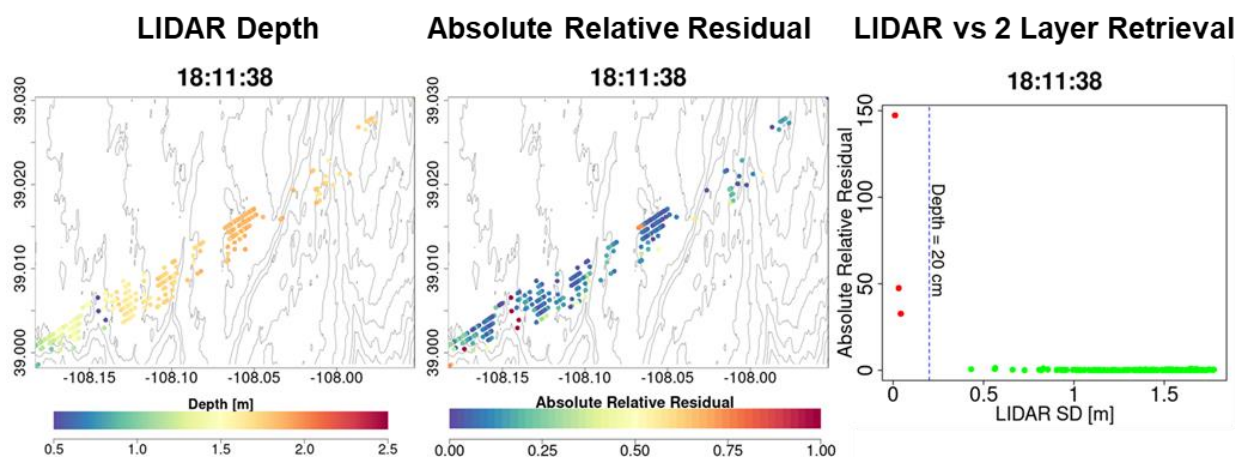
651

652

653 **Table A1** – Same as Table 5 but for resolution of 90 m.

Flight (GMT)	N Layer	Spatial SD μ [m]			Spatial SD σ [m]			MARE SD		BC SD	
		Retrieved	MSHM	LIDAR	Retrieved	MSHM	LIDAR	Retrieved-LIDAR	MSHM-LIDAR	Retrieved-LIDAR	MSHM-LIDAR
18:11:38	1	1.41	1.42	1.40	0.33	0.18	0.26	0.19	0.09	0.90	0.78
18:43:20		1.27	1.39	1.41	0.32	0.19	0.25	0.21	0.08	0.90	0.85
18:59:02		1.48	1.38	1.42	0.37	0.20	0.25	0.21	0.07	0.90	0.82
20:23:38		1.68	1.52	1.66	0.38	0.17	0.19	0.24	0.12	0.66	0.50
18:11:38	2	1.41	1.42	1.40	0.35	0.18	0.26	0.15	0.09	0.95	0.77
18:43:20		1.29	1.39	1.41	0.32	0.19	0.25	0.16	0.08	0.92	0.85
18:59:02		1.41	1.38	1.42	0.35	0.20	0.25	0.15	0.07	0.92	0.82
20:23:38		1.67	1.52	1.66	0.45	0.17	0.19	0.22	0.12	0.76	0.50

654



655

656 **Figure A11** - Analysis of unsuccessful retrievals for pixels with large mean snow depth residuals at 90 m resolution: a) Map of
 657 LIDAR snow depth highlighting in deep blue the locations where very shallow snow is attributed to measurement error. b) Note
 658 spatial agreement between shallow snow depth and very large residuals. c) There are only a few points at the edges of forests and
 659 shallow snow depths that are flagged not successful. The gray elevation contours are plotted every 50 m.

660

661

662

663

664

665

666

667

668

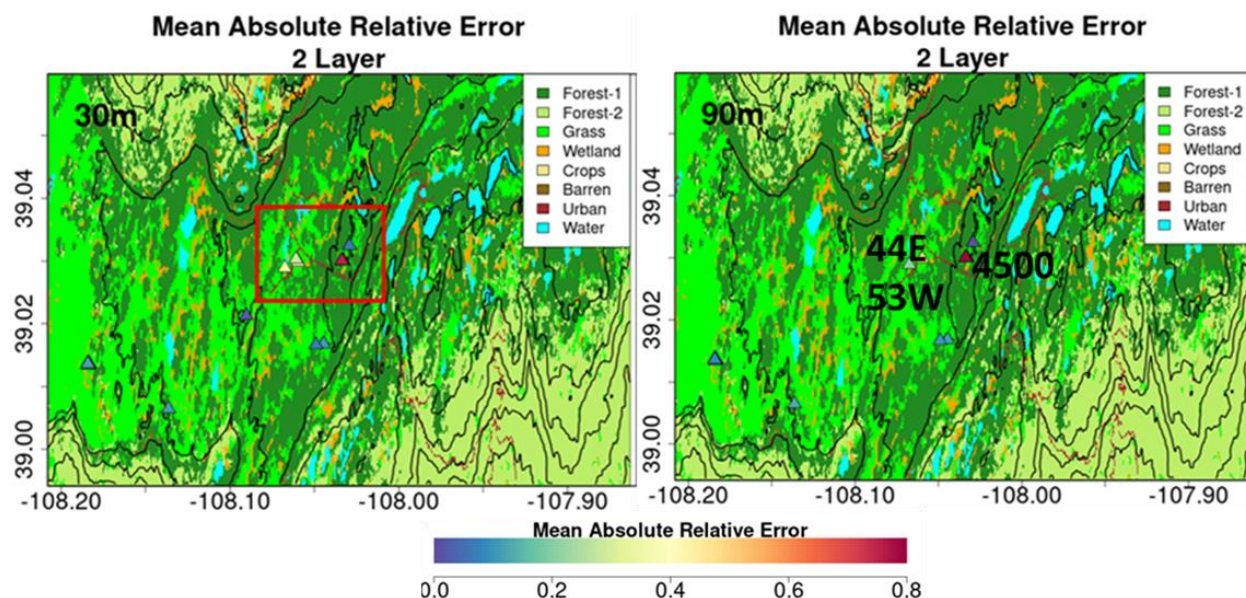
669

670 **Table A2:** Same as Table 7 but for resolution of 90 m.

Date	x	y	Pit SD (m)	Pit SWE (m)	Retrieved SWE (m)		Mean Abs Rel Error		N pixels	Avg. Dist (m)	Pit ID
					1 Lyr	2 Lyr	1 Lyr	2 Lyr			
2/20/2017	-108.184	39.014	1.15	0.368	0.473	0.398	0.29	0.08	4	18	KC1C
2/20/2017	-108.184	39.014	1.19	0.386	0.471	0.397	0.22	0.03	3	12	KC1E
2/20/2017	-108.184	39.014	1.18	0.386	0.473	0.399	0.22	0.03	2	29	KC1N
2/20/2017	-108.184	39.013	1.24	0.414	0.474	0.398	0.15	0.04	3	27	KC1S
2/20/2017	-108.184	39.014	1.3	0.435	0.476	0.399	0.09	0.08	3	47	KC1W
2/22/2017	-108.136	39.006	1.32	0.436	0.572	0.490	0.31	0.12	2	39	29E
2/22/2017	-108.060	39.030	2.10	0.763	0.340	0.384	0.55	0.50	1	43	53W
2/22/2017	-108.044	39.017	1.68	0.566	0.454	0.499	0.20	0.12	1	75	63E
2/22/2017	-108.049	39.017	1.49	0.480	0.521	0.530	0.09	0.10	1	29	63W
2/22/2017	-108.029	39.032	1.66	0.550	0.529	0.553	0.04	0.01	4	47	67N
2/23/2017	-108.067	39.029	2.13	0.761	0.751	0.606	0.01	0.20	1	70	44E
2/24/2017	-108.033	39.030	1.8	0.576	0.718	0.601	0.25	0.04	3	60	0
2/24/2017	-108.033	39.030	1.84	0.598	0.717	0.600	0.20	0.00	2	57	800
2/24/2017	-108.033	39.030	1.80	0.571	0.717	0.600	0.26	0.05	2	55	1390
2/24/2017	-108.033	39.030	1.75	0.566	0.687	0.592	0.21	0.05	1	54	2000
2/24/2017	-108.033	39.030	1.67	0.560	0.687	0.592	0.23	0.06	1	54	2500
2/24/2017	-108.034	39.030	1.12	0.331	0.687	0.592	1.08	0.79	1	62	4500
2/20/2017	-108.184	39.014	1.15	0.368	0.473	0.398	0.29	0.08	4	18	KC1C
2/20/2017	-108.184	39.014	1.19	0.386	0.471	0.397	0.22	0.03	3	12	KC1E
Mean			1.51	0.50	0.56	0.50	0.26	0.13	2.21	42.53	

671

672



673

674 **Figure A12** – Spatial context for snow pits with very large absolute relative errors (MARE) calculated as the mean of the
 675 relative difference between SWE retrievals within 100 m of the snow pit and the values at the snow pit. Locations with very large
 676 errors (orange to red) are inside the red box marked in top plot. Snowpit 4500 is a region of complex land cover including
 677 evergreen forest, a road and a pond. Snowpits 53W and 44E are close to each other on the same side of the road in expansive
 678 grassland.

679

680 **8. Competing Interests**

681 The contact author has declared that none of the authors has any competing interests

682

683 **9. References**

684 Bateni, S. M., Margulis, S. A., Podest, E., and McDonald, K. C.: Characterizing Snowpack and
685 the Freeze–Thaw State of Underlying Soil via Assimilation of Multifrequency Passive/Active
686 Microwave Data: A Case Study (NASA CLPX 2003), *IEEE Trans. Geosci. Remote Sens.*, 53,
687 173–189, <https://doi.org/10.1109/TGRS.2014.2320264>, 2015.

688 Benjamin, S. G., Weygandt, S. S., Brown, J. M., Hu, M., Alexander, C. R., Smirnova, T. G., Olson,
689 J. B., James, E. P., Dowell, D. C., Grell, G. A., Lin, H., Peckham, S. E., Smith, T. L., Moninger,
690 W. R., Kenyon, J. S., and Manikin, G. S.: A North American Hourly Assimilation and Model
691 Forecast Cycle: The Rapid Refresh, *Mon. Weather Rev.*, 144, 1669–1694,
692 <https://doi.org/10.1175/MWR-D-15-0242.1>, 2016.

693 Berliner, L. M.: Physical-statistical modeling in geophysics: Physical-Statistical Modeling in
694 Geophysics, *J. Geophys. Res. Atmospheres*, 108, n/a-n/a, <https://doi.org/10.1029/2002JD002865>,
695 2003.

696 Bhattacharyya, A.: On a measure of divergence between two statistical populations defined by
697 their probability distributions". <https://doi.org/10.3390/rs12203422>, 2020.

698 Cao, Y. and Barros, A.P.: Weather-Dependent Nonlinear Microwave Behavior of Seasonal High-
699 Elevation Snowpacks, *Remote Sens.*, 12, 3422, <https://doi.org/10.3390/rs12203422>, 2020.

700 Cao, Y. and Barros, A. P.: Topographic controls on active microwave behavior of mountain
701 snowpacks, *Remote Sens. Environ.*, 284, 113373, <https://doi.org/10.1016/j.rse.2022.113373>,
702 2023a.

703 Cao, Y. and Barros, A. P.: Indirect Estimation of Vegetation Contribution to Microwave
704 Backscatter Via Triple-Frequency SAR Data, in: *IGARSS 2023 - 2023 IEEE International*
705 *Geoscience and Remote Sensing Symposium*, Pasadena, CA, USA, 3114–3117,
706 <https://doi.org/10.1109/IGARSS52108.2023.10281754>, 2023b.

707 Deems, J. S., Painter, T. H., and Finnegan, D. C.: Lidar measurement of snow depth: a review, *J.*
708 *Glaciol.*, 59, 467–479, <https://doi.org/10.3189/2013JoG12J154>, 2013.

709 Dobson, M., Ulaby, F., Hallikainen, M., and El-rayes, M.: Microwave Dielectric Behavior of
710 Wet Soil-Part II: Dielectric Mixing Models, *IEEE Trans. Geosci. Remote Sens.*, GE-23, 35–46,
711 <https://doi.org/10.1109/TGRS.1985.289498>, 1985.

712 Dobson, M., Ulaby, F., Hallikainen, M., and El-rayes, M.: Microwave Dielectric Behavior of
713 Wet Soil-Part II: Dielectric Mixing Models, *IEEE Trans. Geosci. Remote Sens.*, GE-23, 35–46,
714 <https://doi.org/10.1109/TGRS.1985.289498>, 1985.

715 Hallikainen, M., Ulaby, F., Dobson, M., El-rayes, M., and Wu, L.: Microwave Dielectric
716 Behavior of Wet Soil-Part 1: Empirical Models and Experimental Observations, *IEEE Trans.*
717 *Geosci. Remote Sens.*, GE-23, 25–34, <https://doi.org/10.1109/TGRS.1985.289497>, 1985.

718 Huang, X. and Swain, D. L.: Climate change is increasing the risk of a California megaflood, *Sci.*
719 *Adv.*, 8, eabq0995, <https://doi.org/10.1126/sciadv.abq0995>, 2022.

720 Jacobs, J. M., Hunsaker, A. G., Sullivan, F. B., Palace, M., Burakowski, E. A., Herrick, C., and
721 Cho, E.: Snow depth mapping with unpiloted aerial system lidar observations: a case study in
722 Durham, New Hampshire, United States, *The Cryosphere*, 15, 1485–1500,
723 <https://doi.org/10.5194/tc-15-1485-2021>, 2021.

724 Kang, D. H. and Barros, A. P.: Observing System Simulation of Snow Microwave Emissions Over
725 Data Sparse Regions—Part I: Single Layer Physics, *IEEE Trans. Geosci. Remote Sens.*, 50, 1785–
726 1805, <https://doi.org/10.1109/TGRS.2011.2169073>, 2012a.

727 Kang, D. H. and Barros, A. P.: Observing System Simulation of Snow Microwave Emissions
728 Over Data Sparse Regions—Part II: Multilayer Physics, *IEEE Trans. Geosci. Remote Sens.*, 50,
729 1806–1820, <https://doi.org/10.1109/TGRS.2011.2169074>, 2012b.

730 Kim, E., Gatebe, C., Hall, D., Newlin, J., Misakonis, A., Elder, K., Marshall, H. P., Hiemstra, C.,
731 Brucker, L., De Marco, E., Crawford, C., Kang, D. H., and Entin, J.: NASA’s snowex campaign:
732 Observing seasonal snow in a forested environment, in: 2017 IEEE International Geoscience and
733 Remote Sensing Symposium (IGARSS), 2017 IEEE International Geoscience and Remote
734 Sensing Symposium (IGARSS), Fort Worth, TX, 1388–1390,
735 <https://doi.org/10.1109/IGARSS.2017.8127222>, 2017.

736 Kim, R. S., Durand, M., Li, D., Baldo, E., Margulis, S. A., Dumont, M., and Morin, S.: Estimating
737 alpine snow depth by combining multifrequency passive radiance observations with ensemble
738 snowpack modeling, *Remote Sens. Environ.*, 226, 1–15, <https://doi.org/10.1016/j.rse.2019.03.016>,
739 2019.

740 Kuhnert, P. M. (2017). Physical-statistical modeling. In *Wiley StatsRef: Statistics Reference*
741 *Online*, pages 1–5. Wiley.

742 Li, D., Durand, M., and Margulis, S. A.: Estimating snow water equivalent in a Sierra Nevada
743 watershed via spaceborne radiance data assimilation, *Water Resour. Res.*, 53, 647–671,
744 <https://doi.org/10.1002/2016WR018878>, 2017.

745 Lowman, L., and Barros, A.P.: Investigating links between climate and orography in the central
746 Andes: Coupling erosion and precipitation using a physical-statistical model, *J. Geophys. Res.*
747 *Earth Surf.*, 119, 1322-1353, <https://doi.org/10.1002/2013JF002940>.

748 Manickam, S. and Barros, A.: Parsing Synthetic Aperture Radar Measurements of Snow in
749 Complex Terrain: Scaling Behaviour and Sensitivity to Snow Wetness and Landcover, *Remote*
750 *Sens.*, 12, 483, <https://doi.org/10.3390/rs12030483>, 2020.

751 Martinec, J., Seidel, K., Burkart, U., and Baumann, R.: Areal modelling of snow water equivalent
752 based on remote sensing techniques., XX General Assembly IUGG in Vienna, 1991.

753 Mendoza, P. A., Musselman, K. N., Revuelto, J., Deems, J. S., López-Moreno, J. I., and McPhee,
754 J.: Interannual and Seasonal Variability of Snow Depth Scaling Behavior in a Subalpine
755 Catchment, *Water Resour. Res.*, 56, <https://doi.org/10.1029/2020WR027343>, 2020.

756 Metropolis, N., Rosenbluth, A.W., Rosenbluth, M.,N., Teller, A., and Teller, E.: Equation of State
757 Calculations by Fast Computing Machines. *The Journal of Chemical Physics*, 21, 1087-1092,
758 <https://doi.org/10.1063/1.1699114>, 1953.

759 Mote, T. L., Grundstein, A. J., Leathers, D. J., and Robinson, D. A.: A comparison of modeled,
760 remotely sensed, and measured snow water equivalent in the northern Great Plains: Comparison
761 of Snow Water Equivalent, *Water Resour. Res.*, 39, <https://doi.org/10.1029/2002WR001782>,
762 2003.

763 Musselman, K. N., Addor, N., Vano, J. A., and Molotch, N. P.: Winter melt trends portend
764 widespread declines in snow water resources, *Nat. Clim. Change*, 11, 418–424,
765 <https://doi.org/10.1038/s41558-021-01014-9>, 2021.

766 National Academies of Sciences, Engineering, and Medicine: *Thriving on Our Changing Planet:
767 A Decadal Strategy for Earth Observation from Space*. Washington, DC: The National Academies
768 Press. <https://doi.org/10.17226/24938>, 2018.

769 Painter, Thomas H., Berisford, Daniel F., Boardman, Joseph W., Bormann, Kathryn J., Deems,
770 Jeffrey S., Gehrke, Frank, Joyce, Michael, Laidlaw, Ross, Mattmann, Chris, McGurk, Bruce,
771 Ramirez, Paul, Richardson, Megan, and Skiles, S. McKenzie: ASO L4 Lidar Snow Depth 3m
772 UTM Grid, Version 1, <https://doi.org/10.5067/KIE9QNVG7HP0>, 2018.

773 Pan, J., Durand, M. T., Vander Jagt, B. J., and Liu, D.: Application of a Markov Chain Monte
774 Carlo algorithm for snow water equivalent retrieval from passive microwave measurements,
775 *Remote Sens. Environ.*, 192, 150–165, <https://doi.org/10.1016/j.rse.2017.02.006>, 2017.

776 Pan, J., Durand, M., Lemmetyinen, J., Liu, D., & Shi, J.: Snow water equivalent retrieved from
777 X-and dual Ku-band scatterometer measurements at Sodankylä using the Markov Chain Monte
778 Carlo method, *The Cryosphere Discussions*, 2023, 1-26.

779 Proksch, M., Mätzler, C., Wiesmann, A., Lemmetyinen, J., Schwank, M., Löwe, H., and
780 Schneebeli, M.: MEMLS3&a: Microwave Emission Model of Layered Snowpacks adapted to
781 include backscattering, *Geosci. Model Dev.*, 8, 2611–2626, [https://doi.org/10.5194/gmd-8-2611-](https://doi.org/10.5194/gmd-8-2611-2015)
782 2015, 2015.

783 Rott, H., Cline, D. W., Duguay, C., Essery, R., Etchevers, P., Hajnsek, I., Kern, M., Macelloni,
784 G., Malnes, E., Pulliainen, J., and Yueh, S. H.: CoReH2O, a dual frequency radar mission for
785 snow and ice observations, in: 2012 IEEE International Geoscience and Remote Sensing
786 Symposium, IGARSS 2012 - 2012 IEEE International Geoscience and Remote Sensing
787 Symposium, Munich, Germany, 5550–5553, <https://doi.org/10.1109/IGARSS.2012.6352348>,
788 2012.

789 Sturm, M., Taras, B., Liston, G. E., Derksen, C., Jonas, T., and Lea, J.: Estimating Snow Water
790 Equivalent Using Snow Depth Data and Climate Classes, *J. Hydrometeorol.*, 11, 1380–1394,
791 <https://doi.org/10.1175/2010JHM1202.1>, 2010.

792 Tsang, L., Durand, M., Derksen, C., Barros, A. P., Kang, D.-H., Lievens, H., Marshall, H.-P., Zhu,
793 J., Johnson, J., King, J., Lemmetyinen, J., Sandells, M., Rutter, N., Siqueira, P., Nolin, A.,
794 Osmanoglu, B., Vuyovich, C., Kim, E., Taylor, D., Merkouriadi, I., Brucker, L., Navari, M.,
795 Dumont, M., Kelly, R., Kim, R. S., Liao, T.-H., Borah, F., and Xu, X.: Review article: Global
796 monitoring of snow water equivalent using high-frequency radar remote sensing, *The Cryosphere*,
797 16, 3531–3573, <https://doi.org/10.5194/tc-16-3531-2022>, 2022.

798 Villano, M., Ustalli, N., Dell'Amore, L., Jeon, S.-Y., Krieger, G., Moreira, A., Peixoto, M. N., and
799 Krecke, J.: NewSpace SAR: Disruptive Concepts for Cost-Effective Earth Observation Missions,
800 in: 2020 IEEE Radar Conference (RadarConf20), 2020 IEEE Radar Conference (RadarConf20),
801 Florence, Italy, 1–5, <https://doi.org/10.1109/RadarConf2043947.2020.9266694>, 2020.

802 Wiesmann, A. and Mätzler, C.: Microwave Emission Model of Layered Snowpacks, *Remote Sens.*
803 *Environ.*, 70, 307–316, [https://doi.org/10.1016/S0034-4257\(99\)00046-2](https://doi.org/10.1016/S0034-4257(99)00046-2), 1999.

804